POLITECNICO DI TORINO

Master of Science in Electrical Engineering

Master Thesis Dissertation

Management of a Modular Battery System for Shipboard Application

Relatori
Prof. Michele Angelo Pastorelli
Dr. Fabio Mandrile
Prof. Salvatore Musumeci

Candidato
Simone Mongelli

Settembre 2022

Contents

List of Tables

List of Figures

Introduction

The current maritime industry is the result of a development of about two decades. In this process, shipboard power systems are developing to overcome the challenges of optimal use of energy sources and reduction of environmental impact, especially regarding pollutants and gas emissions. Increasing shipboard developments aim to offer a higher energy efficiency by developing technologies, adding hybrid power generation systems with energy storage system to optimase performance and adopting smart and lightweight materials to increase switching performance and improve power density. In this context, integrated power system is presented, which provides power to all-electric loads. This systems could provide efficient, flexible and environment-friendly. Furthermore the progress of energy storage unit materials makes all electric ships possible, with huge advantages in operational efficiency and costs. The electrification of SPS experiences the changes between ac and dc systems. The SPSs in their infancy are dc distribution networks without advanced power electronics. With the need for ac propulsion motors, the ac SPSs emerged and became popular. In ac SPSs, both generators and propulsion motors are directly connected to the ac bus through breakers, and the service loads are integrated through 50/60 Hz transformers. Therefore, the voltage and frequency control of generators, which supports the ac bus, is vital for the system operation. In recent decades, the development of power electronics, the concerns about fuels and the demands on compact SPSs drove the progress of shipboard generation systems, and research focused on switching to the full electrification of dc ships. Compared to ac distribution, the dc SPS presents a dc bus, and the shipboard power components connect through power converters as the interface to the dc bus. This configuration allows the use of high-speed gas turbines and high-speed generators, and makes it possible to regulate the generator speed without frequency issues . Therefore, the volume and size of SPS can be reduced, as well as the fuel consumption of generators. Furthermore, the dc-SMGs simplify the generator connection without the need of synchronization of phase angle and frequency. Another advantage of dc-SMGs is the replacment of the bulky 50/60 Hz transformers with compact solid-state transformers, which improve the power density. Even with these benefits, the dc-SMGs are a challenge in protection system design. Lacking zero crossing of the current, dc breakers with the capability of disconnecting large current are more complex than ac breakers. Being isolated, a dc-SMG is endowed with limited power mainly generated by synchronous generators and fuel cells (FCs) as the power generation modules (PGMs) to feed the entire system. In the load side, the electric propulsion system accounts for around 80% of the total power demand with large fluctuations, which is one of the main causes for SPS's instability issues. Besides, dedicated loads in ships such as thrusters and radar may bring the voltage oscillation as well. Therefore, the dc-SMGs are weak and the magnitude of perturbations might be high. To improve the quality of service, modern ships are usually equipped with ESS as backup of PGMs to suppress the voltage oscillation. In particular battery energy storage system (BESS) are used, usually a number of battery cells are connected in series and parallel in order to supply higher voltage and higher power to the load. Conventional BESS systems using a single type of battery system where e single dc-dc with a ac-dc or a direct dc-ac interface with a the battery bank is used in microgrid applictions, this system is called centralized battery energy storage system. These systems mainly use new batteries where differences between the cells are fairly minimal. Therefore an active or a passive balancing circuit is tipically employed to overcame any imbalances. **The goal of this thesis is to simulate in PLECS a different type of BESS, a distributed modular BESS with a hierarchical control where every single battery pack have a dedicated modular converter (MC) that take care of battery State of Charge (SOC), state of health (SOH) and other parameters in order to protect battery from deep discharge or overcharging**. In the first chaprer a brefly description about the different configuration in shipboard dc-microgrids is shown with a general description of their component. In the second chapter is described the new distributed BESS topology with all their component.

Chapter 1

Power Architecture of DC-Shipboard Microgrid

Power supply in a ship is usually up to Megawatt, which can't be achived by low voltage SPSs. Moreover, different types of ships have various power supply requirements in terms of energy density, reliability and flexibility.Therefore, it is necessary to study the bus configuration, voltage levels and system configuration of SPSs .

1.1 Bus Configuration and Voltage Levels

There are two types of DC bus architecture in DC networks: unipolar and bipolar topology. In unipolar systems, all the elements are connected to a two-wires, positive and negative, DC bus through converters. The unipolar system is simple but it can't provide redundancy and is weak to protect against any a fault. The bipolar configuration instead has three wires: positive, negative and the neutral ones.Compared to the unipolar one, its advantages respect unipolar are a higher power capacity, an increased reliability, lower transmission losses due to lower current in the return wire and flexibility in the connection between loads and distributed generation. However, since the bipolar architecture can provide different voltage levels, unequal distribution of loads may result in voltage unbalance, which requires a voltage balancer circuit to stabilize the voltage level. Neverthless, most of the existing dc shipboard microgrids use bipolar architecture. Till now, there is no existing standard specifically for DC-SMG defining the dc voltage levels. The system voltage is determined by a lot of factors such as cost, desired generators and propulsion motor drive voltage, converter design, load requirements, cable and bus-bar rating and the fault energy. Basically, the voltage level is determined by the power level and the type of vessel. Recommended MVdc voltage levels for SMG are shown in Table 1.1, with 10% DC bus tolerance.

	MVDC Class	Nominal MVDC Class Rated Voltage	Maximum MVDC Class Rated Voltage
Already Established	1.5	1.5 or ± 0.75	2or ± 1
	3	3 or ± 1.5	5 or ± 2.5
Future Design	6	6 or±3	10 or± 5
	12	12 or ± 6	16 or±8
	18	18 or ±9	22or ±11
	24	24 or ±12	28 or ±14
	30	30 or ±15	34 or ±17

Table 1.1: Recommended MVDC Voltage Classes (KV) [1]

1.2 System Architecture

- *Radial Distribution*

  Radial distribution, shown in Fig. 1.1, is a conventional configuration recommended and used in SMGs. Typically, there are two dc buses that distributes the power to the consumers. Power sources are distributed simmetrically and feed each DC bus. The port and starboard propeller are powered by two DC buses separately, while two DC buses supply the onboard service loads for higher reliability.The radial scheme is the simplest one and is also cost-efficient. However this solution becomes bulky when the number of loads increases and it isn't flexible when a fault occurs in dc buses.

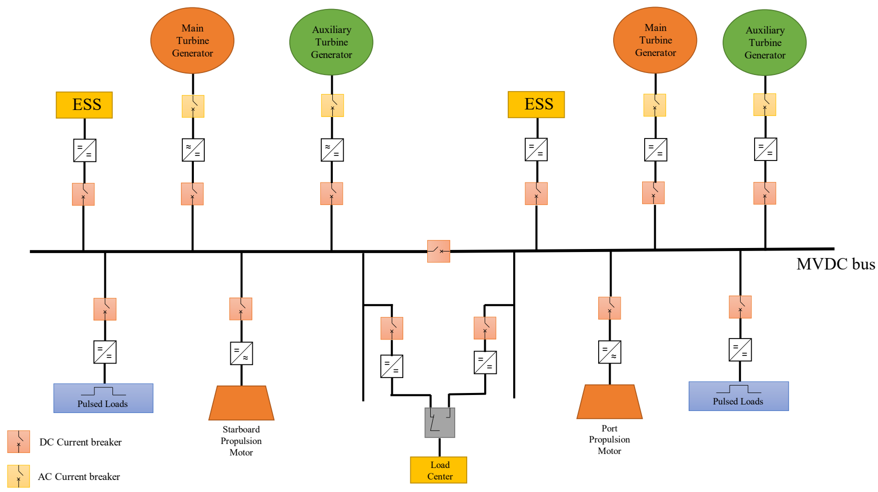

Figure 1.1: IPS based on Radial distribution.

- *Zonal Distribution*

  This configuration has become the U.S. navy standard. As shown in Fig. 1.2, in this case the loads are divided in n zones, each one is fed by two connections from the buses and controlled independently. This configuration guarantees redundancy for loads from two longitudinal DC buses. Every load center has connections with both the port and starboard buses and when a fault occurs on one side, the vital load in the zones will automatically shift their power sources to the healthy opposite bus. The longitudinal bus allows isolating faults with the minimum affected areas using coordinated protection systems with a communication network. Moreover, the subdivision of the loads from bow to stern along the ship reduces the cable needed, lowering the cost and impacts of the cables.

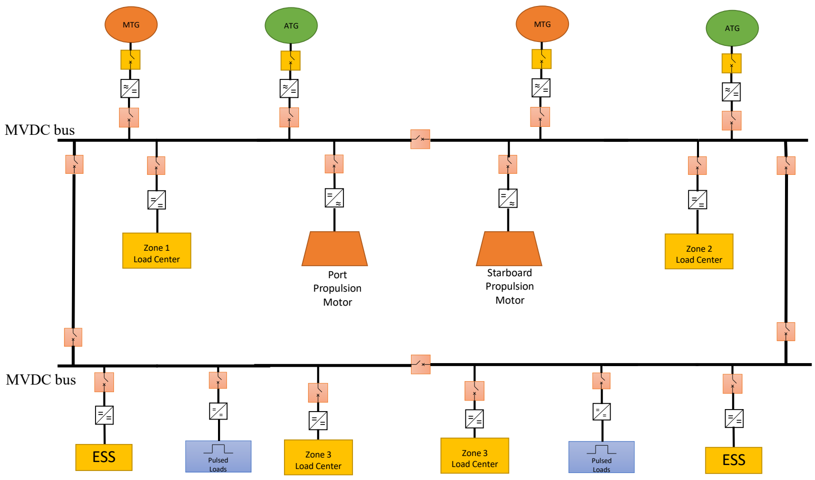

Figure 1.2: IPS based on Zonal distribution.

- *Ring Distribution*

This configuration is used in few cases. A typical ring distribution is shown in Fig. 1.3. In ring distribution, the bus-tie switches connecting DC buses are kept closed in normal operations, making the DC bus a loop. As the zonal configurations, the ring architecture has higher survivability and reconfigurability than radial ones. When a single fault occours in DC bus, the ring distribution isolates the fault through the nearest circuit breakers and keeps the remaining part working as normal. However, one of the differences from zonal distribution is that each load center in ring distribution has only one link to the bus, so the vital loads are susceptible to faults. The ring distribution is like a transition between radial and zonal ones, and it is ararely used in SMGs.

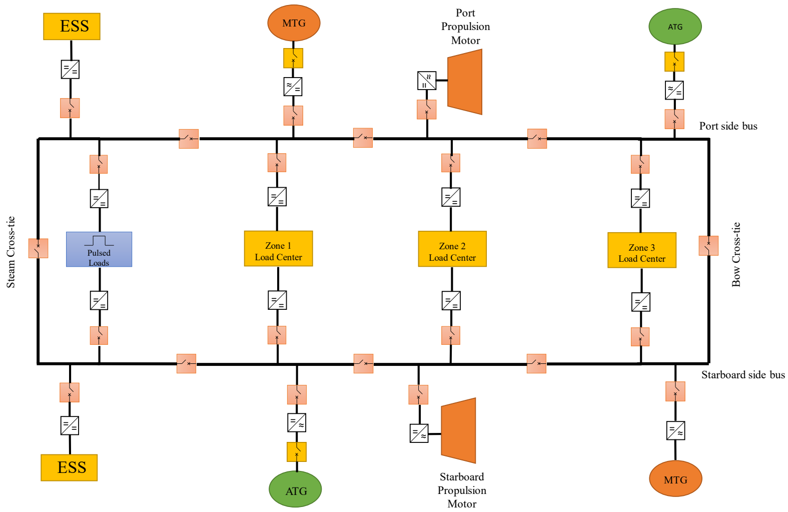

Figure 1.3: IPS based on Ring distribution.

A qualitative comparison on radial, zonal and ring distribution is shown in Table 1.2, based on typical aspects such as reliability, survivability, complexity and reconfigurability. Radial architecture needs less breakers and its structure is the simplest, while on the contrary, the reliability, reconfigurability and survivability are the worst. The zonal has the best performance in these three features, whereas the price and complexity are higher as also the number of breakers. Ring configuration has the medium level in this comparison. In conclusion the radial scheme can be used in small ships with few components and in the cases in which the required reliability on the system is not very high. For large ships with high requirement on system reliability and survivability, zonal and ring schemes are preferred for better personal and good safety instead.

1.3 Energy Storage System in Ships

The ESS has an important role and they are widely used in ships. The ESS can bring five benefits: spinning reserve, peak shaving, network resilience and stability, shaft

	Radial	Zonal	Ring
Bus Scheme	Two buses connected by one breaker	One ring bus with $2n + 2$ breakers	One ring bus with 6 breakers
Reliability	Low	High	Medium
Survivability	Low	High	Medium
Reconfigrability	Low	High	Medium
Complexity	Low	High	Medium

Table 1.2: Comparison of Radial, Zonal and Ring Distribution

generator load transfer and harbor operation. Due to the large inertia of the generation system, fast dynamics can't be regulated by the prime mover of genset, while ESS can quickly meet the load domands. In case the generaion system fails, or during the short period of fault isolation of the interruptible parts, ESS can supply as a backup power source. Moreover, voltage instability caused by pulsed loads with a considerable high-power ramp rate can be suppressed by high-power density ESS. I n SMG, the ESSs can be based on a group of tecnologies including battery, ultra-capacitor (UC), flywheel and superconductors. The choice of ESS technology depends on the power range, power density, cost, charge/discharge time etc. The batteries and the UCs are integrated into the DC-SMGs with the interface of a dc-dc converters, while the flywheels and superconductors are connected throught ac-dc converters.

- *Battery Energy Storage System*

  The battery energy storage system (BESS) is a popular solution in SMG for high power and long term demands. Usually, lithium-ion battery is a good option due to its high energy density, low self discharge rate and long lifetime. A BESS can be integrated into the DC-SMG distribution throught a bidirectional converter. Normally, batteries are integrated by organizing multiple battery cells in series and parallel to built a storage unit in matrix. A centralized battery storage system checks the cell parameters such as SOC, temperature, voltage and manage the power flow. However, this type of configuration has problem in voltage sharing, over charge/discharge and efficiency iussies. To solve this problem, distributed BESS is proposed in recent years, in which every battery cell has a personal dc/dc converter that regulate the output power.

- *Ultra – Capacitor Energy Storage System*

  Due to its lower internal resistance, ultra capacitor(UC) has a small time constant, allow it to deliver a high charge/discharge ramp rate. However, the energy density in the UC is relatively low, while batteries have benefits in energy density. Consequently, hybrid energy storage system (HESS), with the combination of batteries and UCs, not only can reach the long term load demand but also reduce peak power stresses on the battery packs, and it is also suitable to satisfy peak power demand for pulsed loads and transient load varation.

- *Flywheel Energy Storage System*

  Since ships operate in various operating conditions, fast response high-power ESS is required. Flywheels ESS (FESS) can not only meet this requirement but also has the vantages of low manteinance, high energy efficiency long lifetime and environment-friendly. However, it can not be ignored that FESS has the drawbacks of high self discharge rates. The most common application for FESS are for uninterruptible power supplies and power quality improvement. Tipically, FESS is a supply device that stores energy in form of kinetic energy in a rotating flywheel connected to the shaft of an electric machine. The FESS structure, shown in Fig. 1.4 containing a rotor (flywheel), shaft, motor/generator, and power electronic interface. The amount of stored energy depends on the form, mass and rotation speed of the flywheel.

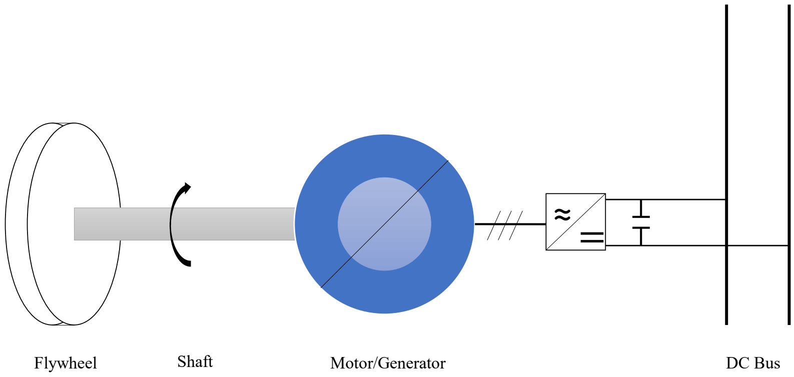

Figure 1.4: Structure of the flywheel ESS.

- *Superconductingl Magnetic Energy Storage System*

  Superconducting magnetic ESS (SMESS) is a technology that stores energy within the magnetic field generated by the current flowing throught a coil comprised of superconducting wire with near-zero loss of energy. Simolar to the other ESS, SMESS also has the capability of frequent and rapid charging and discharging with an efficiency over 95%. A tipical SMESS consists of a criogenically cooled superconducting coil and power conditioning system, as shown in Fig.1.5 Due to the cooling system required, the initial cost of SMESS is very high, and a large amount of power is needed to mantein the cryogenic temperature.

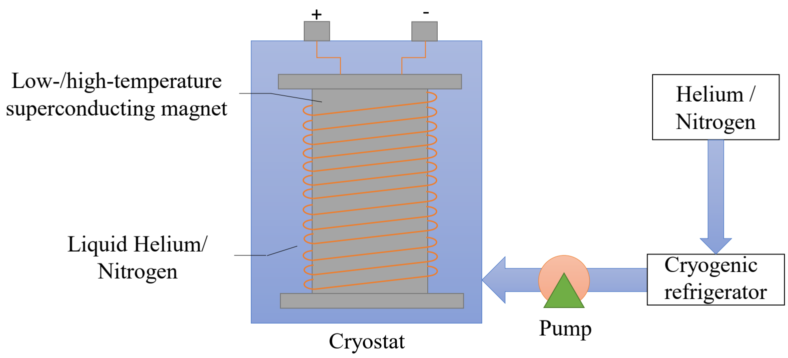

Figure 1.5: Superconducting magnetic ESS.

- *Hybrid Energy Storage System*

  By analyzing features of various ESS type, it is obvious that there is no perfect option being able to meet all the requirement in ship applications. Different energy storage systems are suitable for compensating different power fluctuation range. A quantitative comparison shows that BESS has relatively high energy ratings but the maximum power is shorter and the response time is longer than the other technologies. On the other hand, UC, FESS and SMESS havethe capability to provide high power in very short time but the energy ratings is lower than BESS. So Hybrid energy storage system (HESS) is usually adopted to fulfill the needs in ships. The most common combination batteries and UCs, that can provide high energy density from batteries.

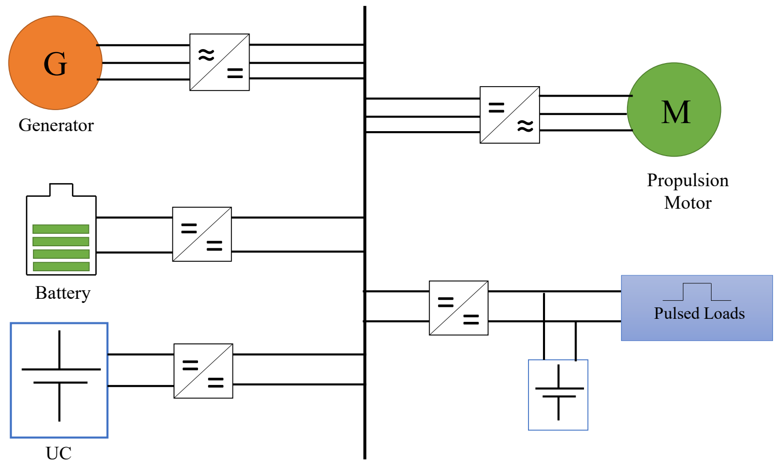

Figure 1.6: Block diagram of dc-SMG with battery/UC HESS.

Chapter 2

Battery Energy Storage System Configuration

In this Chapter the new topology is presented with a brefly explaination about the component that formed the new system such as the converter used, with his operation and current control, and the model of battery used in the simulations.

2.1 Centralized BESS

The BESS have so an important role in dc-MGs as ships, in order to garantee stability and increases the energy stability of the system. Normally, a conventional BESS, as shown in Fig. 2.1, is formed by a multiple cell banks that buld a matrix. This system usually feeds the DC bus throught a centralized dc-dc bidirectional converter. Ideally, the cells that form the matrix are identical, in practice due to manifacturing tolerances, different self discharge rates, uneven operating temperature across the battery cells and nonuniform aging process will create mismatches. As a result, the battery SOC in series will diverge from one another during charging/discharging operationand this will cause a misuse of the battery energy and overdischarge/overcharge for some of the battery cells. This may create serious problems such as overheating, battery deterioration and in the worst case scenario they could catch fire. To avoid this battery imbalance iussie, usually a cell balancing circuits are usually utilized as an integral part of the battery management system (BMS) in order to minimize the imbalances. As we can see in Fig. 2.1, a high power dc-dc converter is utilized to control the dc bus voltage to the rest of the system. To reach the SOC balancing among the string, cell is equipped with an balancing circuit (BC). In general we can divide balancing circuit in two categories: dissipative and energy-recovery cell balancing schemes. The dissipative balancing scheme is usually a shunt resistor and a switch in parallel with each battery cell. The excess in energy is dissipated trought the shunt resistors in the form of heat. This scheme has the advantages of low cost and easy implementation. However, this scheme lowers the efficiency of the system and generate more heat to dissipate. The energy recovery cell balancing scheme, instead, achives cell balancing by transferring the excess energy between the battery cells through switched-capacitors circuit. However with this type of balancing circuit, energy is only transferred between adjacent battetry cells. If the energy is trasferred from the battery cell on one end to the battery cell on the other end, a significant portion of energy can be lost along the energy transfer path.

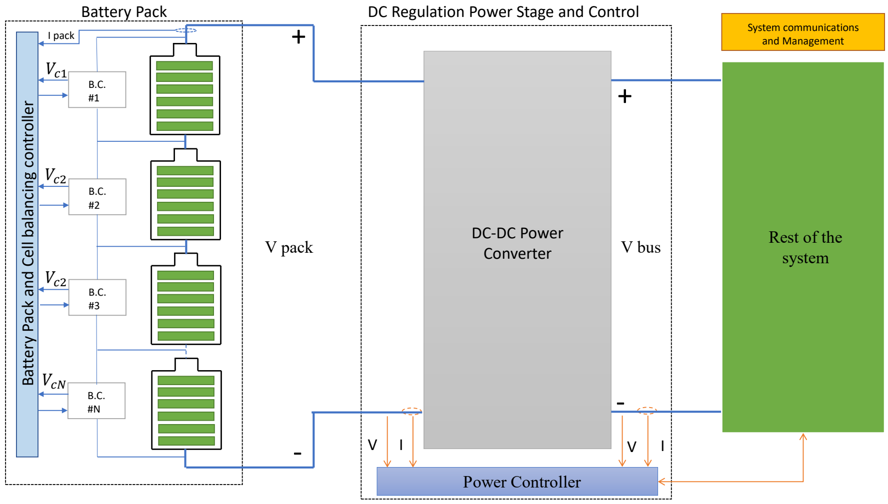

Figure 2.1: Simplified block diagram of a conventional Centralized BESS.

2.2 Distributed Modular BESS

In this section the new type of BESS is presented. In this one rather than connecting the ESS trough a high power dc-dc converter, rated at Y. The system is decoupled in more ESSs which are connected to a lower power dc-dc converter rated at Y/N, where N is the number of of ESSs or Sub Modules (SMs). As shown in Fig. 2.2 the output of every ESS module is connecting in series in order to achive a higher dc-bus voltage.The control is guaranteed by a a hierarchical control, where the Master controller, thanks to the information that he recives from the various slave in every string, will divide, following a special alghoritm, the power between the strings.

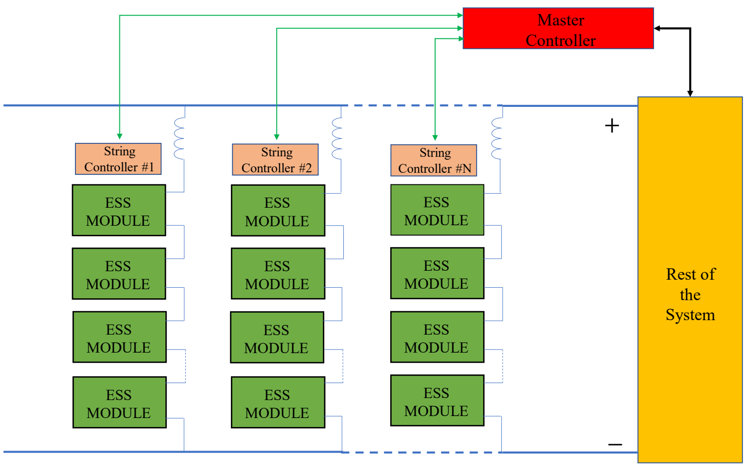

Figure 2.2: Simplified block diagram of the proposed BESS topology.

2.2.1 Elementary Bidirectional DC-DC Converter

The converter in every BESS module is a bidirectional switching cell that can be obtained by combining the two elementary unidirectional DC-DC converter, Buck and Boost, as shown in Fig. 2.3 , the connection of transistor T_1 and T_2 is in parallel with a voltage source, so they shall never be simultaneously in ON state to avoid short-circuit of V_{in}.

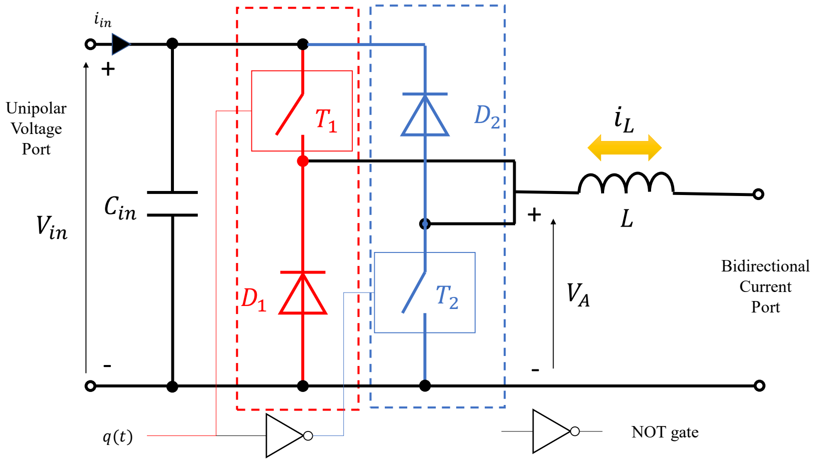

Figure 2.3: Topology of a Bidirectional DC-DC Converter.

In Fig. 2.4 is shown the operating conditions when the switch $T1$ is ON, instead in Fig. 2.5, is shown the operating conditions when the switch T_2 is turned ON. As we can see, for an ideal bidirecgtional cell, the output voltage depends only on the input voltage V_{in} and the switching function $q(t)$ and the sign of power depends only on the sign of output current [2].

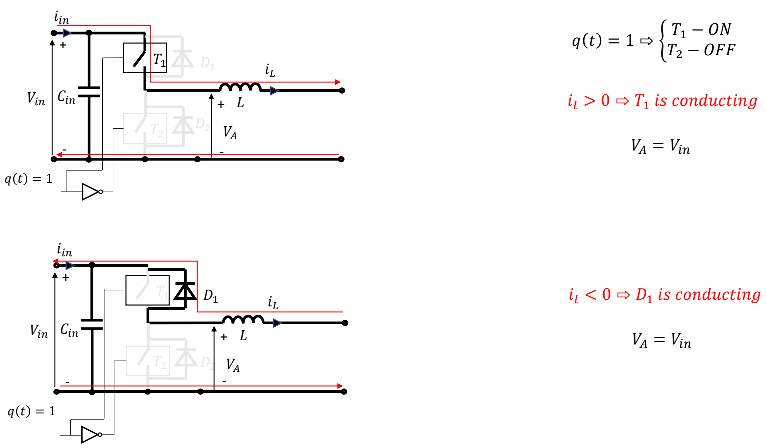

Figure 2.4: Bidirectional DC-DC Converter Operation when T_1 is ON.

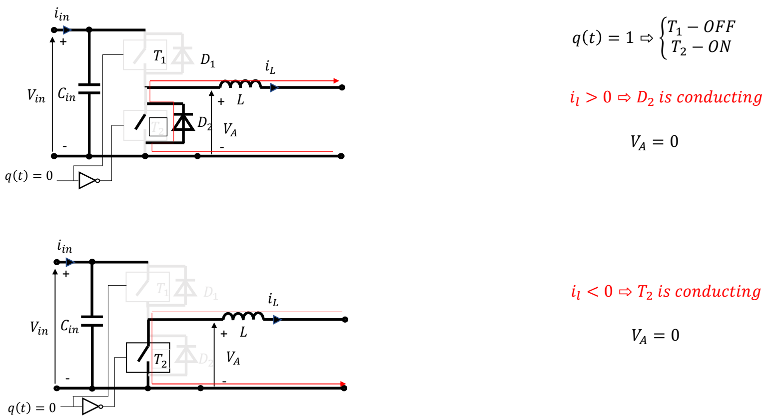

Figure 2.5: Bidirectional DC-DC Converter Operation when T_2 is ON.

This bidirectional switching cell is used as interface between the ESS and the rest of the system and depending of the case and the sign of the current we can charge or discharge the battery.

In this work the switching function $q(t)$ of power switches are generated by a PWM modulator with a unipolar triangular waveform as a carrier at frequency $f_{sw} = 1/T_{sw}$ where T_{sw} is th switching period, which is compared with a control signal v_c as shown in Fig. 2.6.

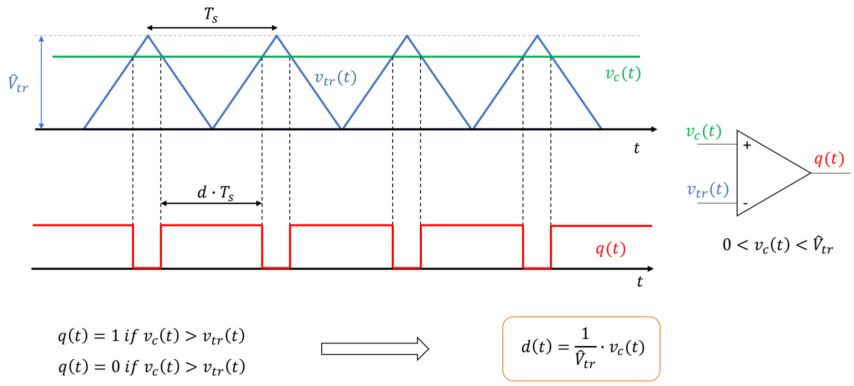

Figure 2.6: Simmetrical PWM waveforms.

2.2.2 Simulation of an Ideal Bidirectional DC-DC Converter

In this section it will be shown a simulation of an ideal Bidirectional DC-DC Converter. In our simulations the peak of the triangular waveform is set to one, so the control signal $v_c(t)$ in our case is equal to the duty-cycle $d(t)$. In tihs case we are considering an ideal bidirectional converter so we don't need to consider a dead-time to avoid the short circuit of V_{in}. In Fig. 2.7 is shown the system simulated in PLECS, in this case we will consider an indeal voltage source as V_{in}, so we don't need a and also an ideal voltage source as V_{out}.

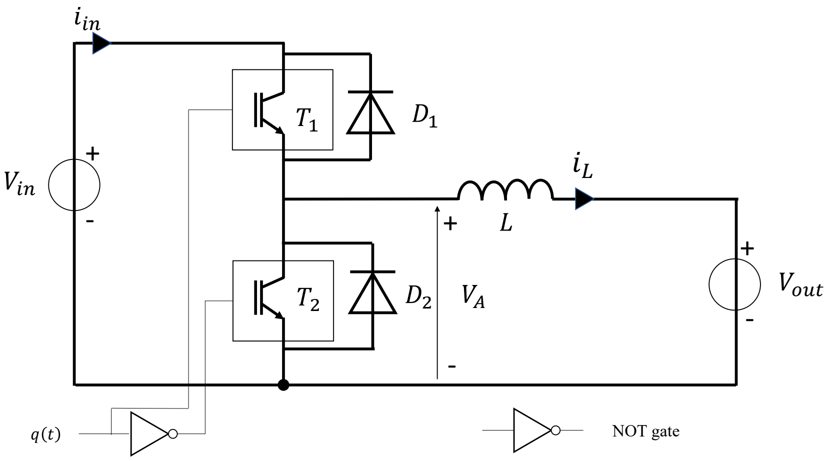

Figure 2.7: Scheme of the Bidirectional DC-DC Converter simulated.

The current control scheme is the same of a Buck Converter. In this case, instead, the current current could be positive and negative so the discontinuous conduction mode (DCM) is avoided. In Fig. 2.7 is shown the system simulated in PLECS, in this case we will consider an indeal voltage source as V_{in}, so we don't need a and also an ideal voltage source as V_{out}. In Fig. 2.8, a block diagram of the current control is shown. The calibration of the control is quite simple because the system contains only one pole [3].

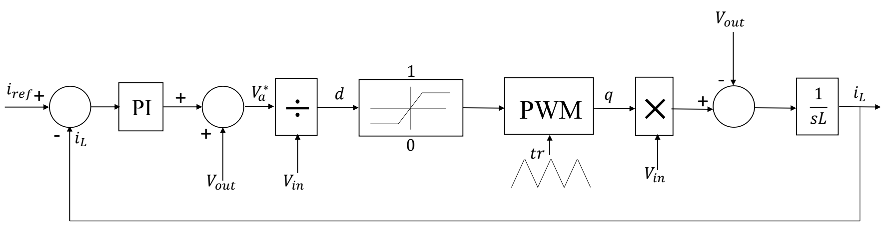

Figure 2.8: Current Control Block Diagram for a Bidirectional DC-DC Converter.

The calibration of the control is quite simple because the system contains only one pole, it is shown in (2.1). The proportional gain is set to determinate the bandwidth, instead the integrative gain is set to obtein a sufficient phase margin and guarantee stability and a good damping.

$$\begin{cases} K_p = \omega_b L \\ K_i \ll K_p \omega_b \end{cases} \tag{2.1}$$

The I_{out} is formed by two components, a DC component equal to I_{ref} and a AC component (ripple) due to commutation. The inductance has the important role to reduce the value of peak to peak curren caused by commutation and in case of fault to limitate the current rising. The peak to peak value, it is a function of f_{sw}, V_{in}, V_{out}, d and L, as showen in (2.2) :

$$\Delta I_{out} = \frac{1}{L} \cdot (V_{in} - V_{out}) \cdot (d \cdot T_{sw}) = \frac{1}{L} \cdot V_{out} \left[(1-d) \cdot T_{sw}\right] \tag{2.2}$$

Usually the peak to peak value is set as a percentage of the I_{ref}, and is a specification parameter. In this case we set the parameter as 10% of I_{ref}. So this value is set according to (2.3):

$$L = \frac{1}{0.1 \cdot I_{ref}} \cdot (V_{in} - V_{out}) \cdot (d \cdot T_{sw}) = \frac{1}{0.1 \cdot I_{ref}} \cdot V_{out} \left[(1-d) \cdot T_{sw}\right] \tag{2.3}$$

In Table 2.1, there are the parameter set for the dimonstrative simulation to show the trend of the main electrical quantities. The I_{ref} is set as a simmetrical square wave.

In Fig.**??**, we can see that the current follows correctly the reference.

Simulation Parameters	
I_{ref}	10 A
I_{ref} frequency	1 Hz
V_{in}	24 V
V_{out}	10 V
f_{sw}	10 kHz
L	0.583 mH
ω_b	$1000 \cdot 2\pi$ rad/s
K_p	$\omega_b L$
K_i	$0.5\omega_b K_p$

Table 2.1: Parameters Value for Bidirectional DC-DC Converter's Simulation

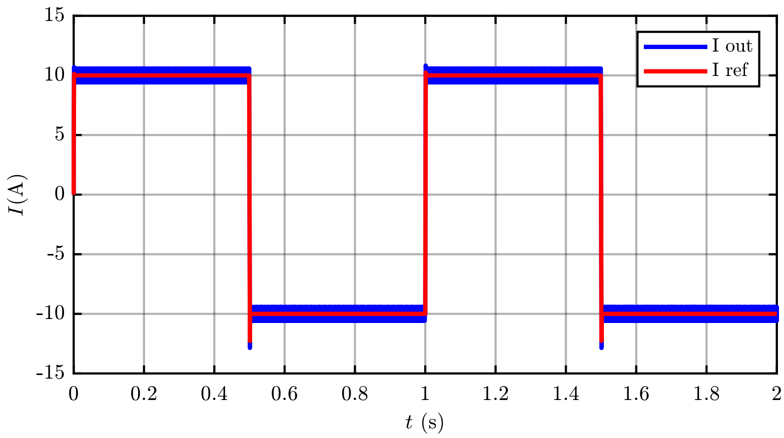

Figure 2.9: Current Waveform with a square waveform reference with $I_{ref} = 10A$.

If we zoom the figure, as in Fig. 2.10, we can see the two components in I_{out} mentioned before. We see clearly the ripple caused by commutation and its value is $\Delta I_{out} = 0.1 I_{ref}$.

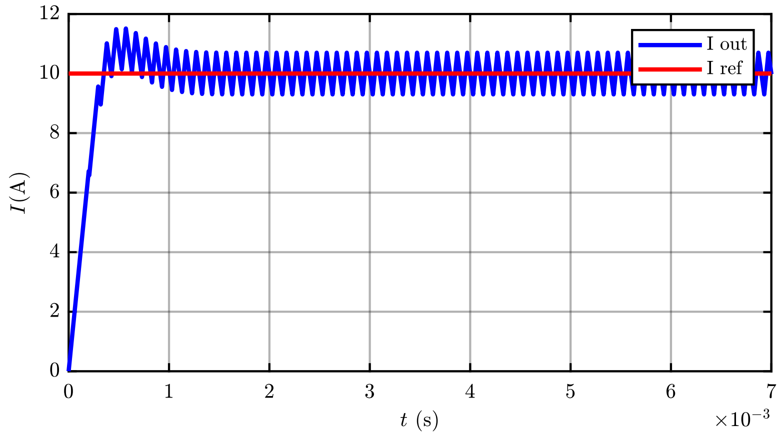

Figure 2.10: Current Ripple with $I_{ref} = 10A$.

The carrier is an unipolar having the peak set to unity so the v_c is equal to the duty cycle d. In Fig. 2.11, are shown in sequence, the Carrier with the duty cycle and the commands of high switch and low switch.

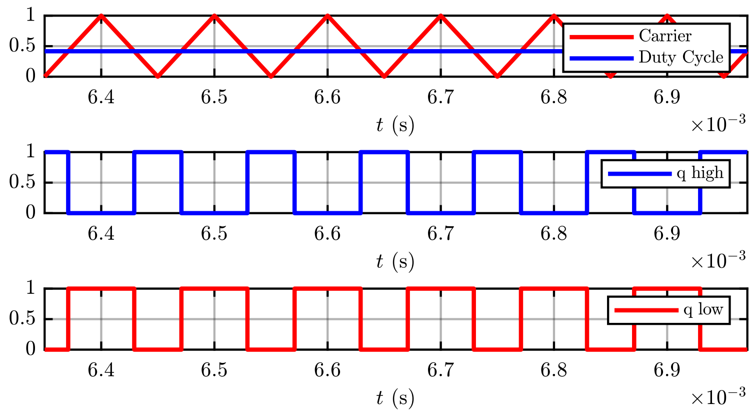

Figure 2.11: Waveforms of Carrier and Duty Cycle, q_{high} and q_{low}.

2.2.3 Digital Control Algorithm

In this simulation the control is implemented as a digital control [4]. All the quantities are treated as digital, every time step a triggered sub-system is called, like a interrupt service routine (ISR) implemented in a μC, and the control code is executed. All the quantities are measured, calculated and updated at every time step. The execution of the output, instead, is postponed to the next time step, in Fig. 2.12 is shown how the system works.

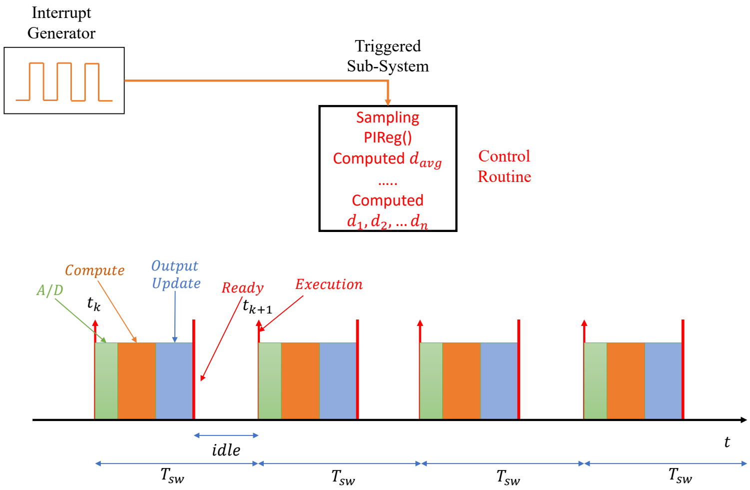

Figure 2.12: Discrete Time Control Routine.

The interrupt is called synchronized with the PWM time step T_{sw}, in order to have a correct measurement of I_{out}, in fact in a dc-dc converter if the sampling is done in the peaks of the carrier, when no switching is taking place, the ripple caused by switching is avoided and the sampling is done exactly in the average value of the current, as shown in Fig. 2.13.

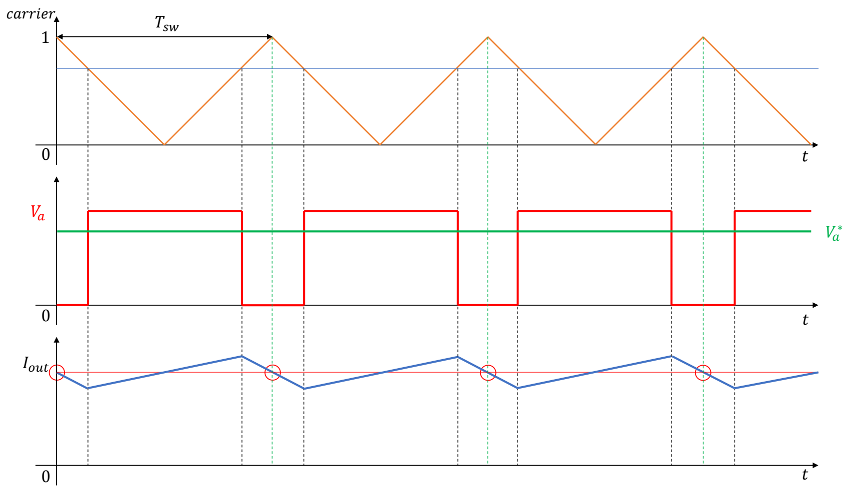

Figure 2.13: Current Sampling in DC-DC converter.

2.2.4 PLECS Battery Model

This section explains the battery model implemented in PLECS [5] for simulations. For our goals we do not need a complex physic-based model but for our scope we will use an electrical model offered by PLECS. A model example offered by PLECS is based on a CGR18650CG 3.6V 2250mAh Panasonic cell. The behaviour of the cell is shown in Fig. 2.15, when the battery is fully charged, the output voltage is near to $4.1V$. During discharge, the output voltage decreases in an approximately linear behavior until the energy has been depleted. Below 3.0V, the cell can be assumed to be empty and must be recharged. The concept is to model the cell using an internal voltage and an internal resistance, as shown in Fig. 2.14. The reference internal voltage is a non-linear function of the state of discharge.

$$V_{cell\ ref} = f\,(SOD) \tag{2.4}$$

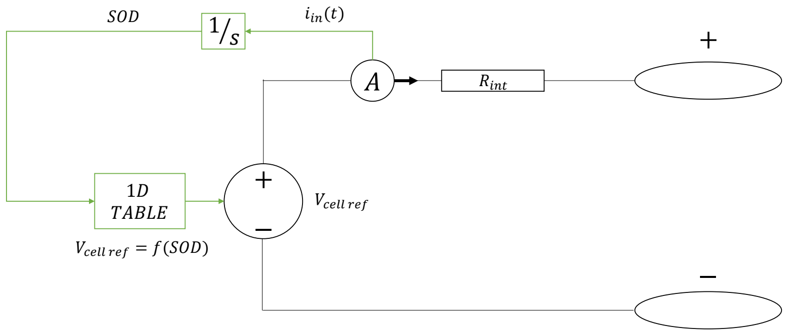

Figure 2.14: Battery Model implemented in PLECS.

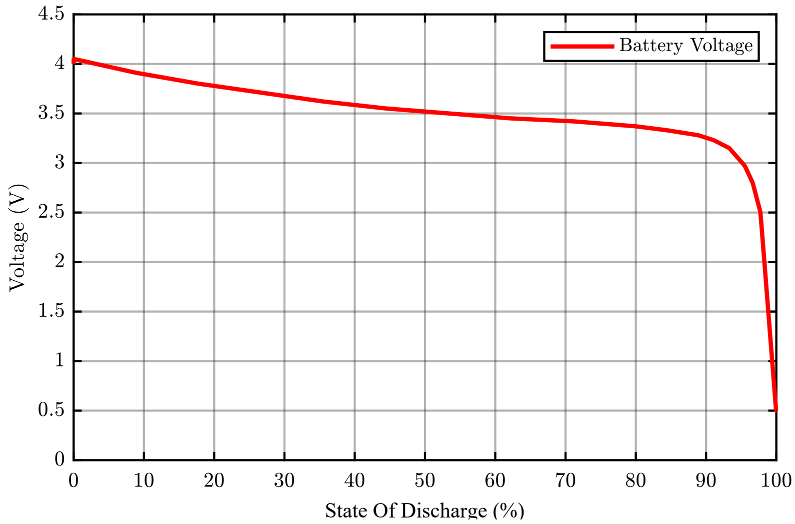

Figure 2.15: Voltage Characteristics of CGR18650CG Model.

And the state of discharge is showed in (2.5), where C is the nominal capacity of the cell in Ah and $T = 3600s$.

$$SOD_{\%} = \frac{100}{C \cdot T} \int_0^t i(t)dt \tag{2.5}$$

The data for modelling $V_{cell\ ref}$ is based on a curve measured at constant $T = 20°C$

and $i(t) = 2.15\ A$. The initial internal resistance is calculated from the manufacturers voltage curve and for our application it will be considered constant, for this type of cell the value is 0.07 Ω.

Chapter 3

Control Algorithm of the System

In this Chapter it will be shown the alghoritm implemented to control the current of the system. A general explanation is presented considering only a string with n modules and then simulation results considering three ideal modules.

3.1 General Presentation of a String Control Algorithm

We will consider the system shown in Fig. 3.1, there is only one string with n ESS module in series.

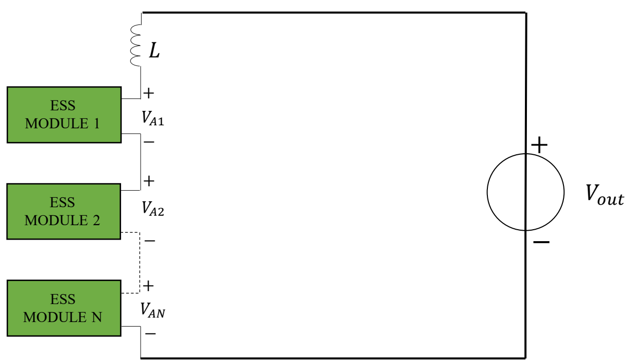

Figure 3.1: One-String System Structure.

The control scheme is mainly divided into two parts. The first part involves the calculation of a duty average d_{avg}, which will be calculated by the master controller which in this case having only one string will also be the string controller, the d_{avg} will be used for current control. The second part will involve the calculation of the individual d_i of the various converters in the string [6], which will go to control the output current from the various voltage generators. The dynamic equations can be written as follow:

$$L \cdot \frac{dI_{out}}{dt} + V_{out} = d_{avg} \cdot \sum V_{in,i} \qquad \forall i = 1, ..., n \tag{3.1}$$

$$d_{avg} = \frac{\sum V_{a,i}}{\sum V_{in,i}} = \frac{\sum V_{in,i} d_i}{\sum V_{in,i}} \qquad \forall i = 1, ..., n \tag{3.2}$$

$$i_{in,i} = I_{out} \cdot d_i \tag{3.3}$$

Therefore, the d_{avg} is the wheighted average of the entire system. Every single d_i is calculated as wheiged portion of d_{avg}, as shown in (3.4):

$$d_i = n \cdot d_{avg} \cdot \frac{V_{in,i}}{\sum V_{in,i}} \tag{3.4}$$

The block diagram for calculating d_{avg} is the same as for the single bidirectional dc-dc converter, as shown in Fig. 3.2 , with some modifications due to the different parameters.

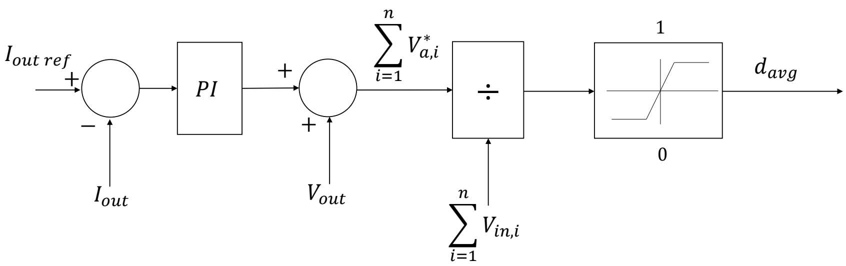

Figure 3.2: d_{avg} Block Diagram.

The calculation of the various duties d_i of the individual converters will be derived from the d_{avg} through a division proportional to the input voltages $V_{in,i}$ in the various converters as shown in Fig. 3.3.

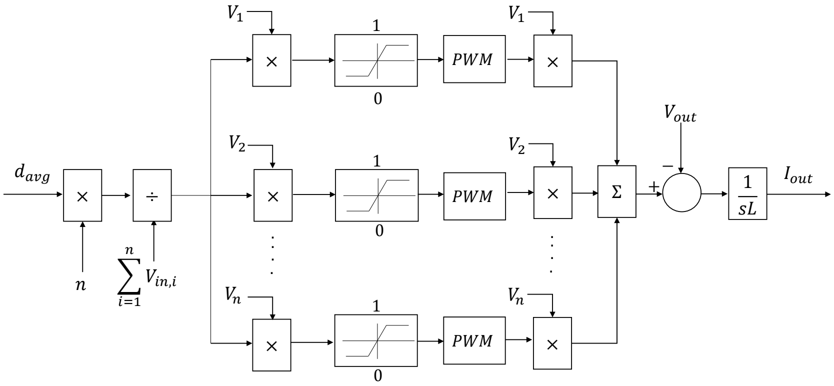

Figure 3.3: Block Diagram of the System with One String.

A reduced system with three modules with ideal generators, each with three different voltages, was considered for simplicity in order to show the trend of the various system quantities. In this case, the sizing of the string output inductance is identical to the two-way converter simulation shown in the previous chapter, but in this case the input voltage considered will be equal to the sum of all the ideal voltage generators. The output considered is always an ideal voltage generator. The parameters chosen for the simulation are shown in Table 3.1. In this case, the trend of the reference current is the same as in the simulation carried out in the previous chapter. The inductance value was chosen to obtain an output current ripple of 10% of the reference current I_{ref}.

Simulation Parameters	
I_{ref}	100 A
I_{ref} frequency	1 Hz
V_{in1}	80V
V_{in2}	70 V
V_{in3}	50 V
V_{out}	100 V
f_{sw}	10 kHz
L	5 mH
ω_i	$1000 \cdot 2\pi\ rad/s$
K_p	$w_b \cdot L$
K_i	$0.2 \cdot w_b \cdot K_p$

Table 3.1: Parameters Value for Bidirectional DC-DC Converter's Simulation

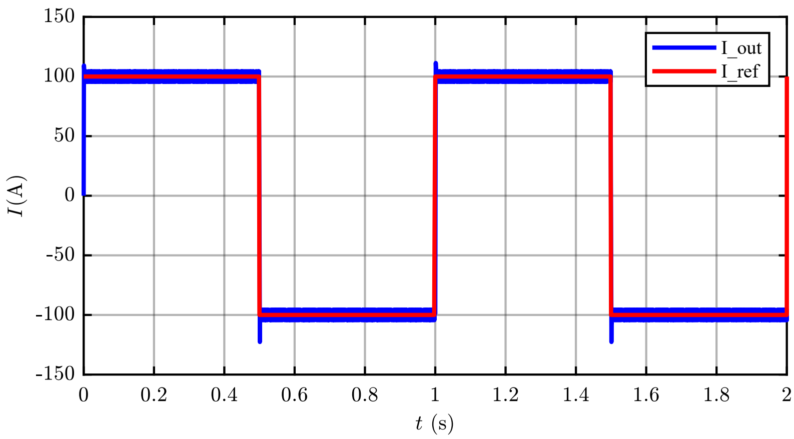

Figure 3.4: Current Waveform with different voltage sources.

If we see the waveforms more closely so that we can see in Fig. 3.5 the current ripple. It can be seen that the ripple amplitude is less than 10% of the reference current. This is due to the waveform of the voltage output from the various modules with their own converters

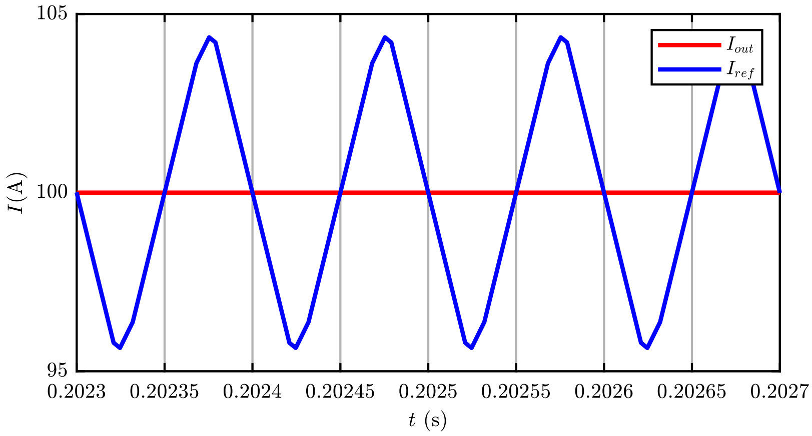

Figure 3.5: Current ripple with different voltage sources.

In fact, as opposed to a single converter with a single duty, the three converters working with different duty will generate a voltage waveform at the output that is different from a square wave, but the voltage will be very similar to a staircase ramp. Because of this particular voltage waveform, the current ripple will not be perfectly triangular. Fig. 3.6 shows the different duties proportional with voltage compared with the carrier, and Fig. 3.7 shows the voltage waveform generated by the different commands

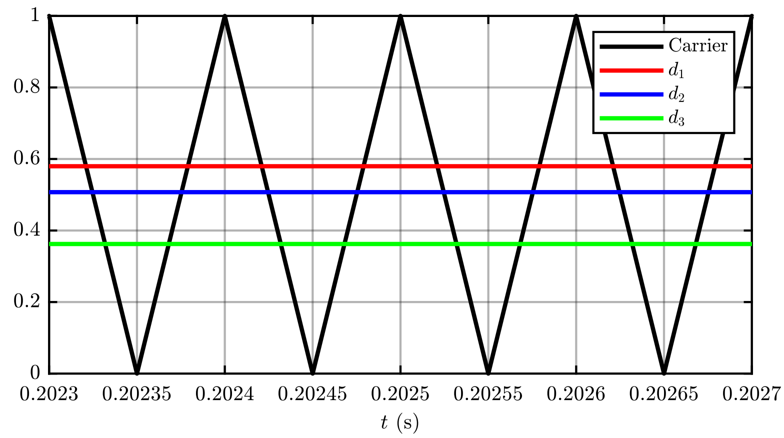

Figure 3.6: Carrier with different duties.

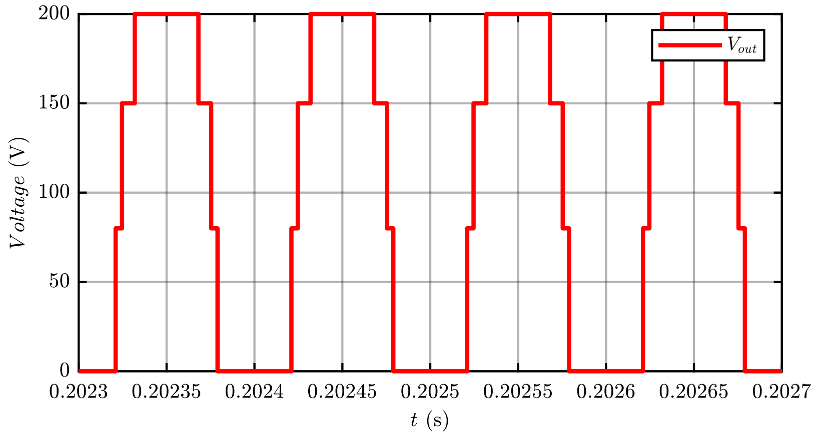

Figure 3.7: Voltage output with three different voltage sources.

3.2 Phase Shifting and Current Ripple

This section will show some control modifications thanks to the modularity of the system. As we have seen, the system can consist of n ESSs connected in series. This allows the system to be scaled to various voltage and power levels. In order to control this system, there are two types of configurations: a centralized control and a distributed control. In centralized control, a single microcontroller will perform all the operations and calculations necessary to operate the system. The microcontroller will therefore need high computing power and must be able to generate a large number of signals. In contrast, in a possible distributed control, each module has its own controller along with the master controller. A communication network must therefore be created between the master controller and the controllers of the various modules. In this type of control, the master will have to take care of controlling the current loop and the various measurements and generating the various duty cycles to be sent to the module controllers. The module controllers will be responsible for generating the PWM signals to be compared with the duty and consequently for generating the signals of the switches, in addition they will be responsible for measuring the input voltages[7]. One of the main problems with distributed control is due to communication caused by component drift or lack of synchronization of the PWM signals of the various controllers [8]. The carrier used for the PWM signal is generated by an internal counter in the microcontrollers, which will then be compared with the duty sent by the master controller. However, it is necessary for the PWM signals to be properly synchronized with each other and start counting at the same time. In reality, however, this condition is not always met without a possible synchronization signal. In fact, there may be delays between the various microcontrollers and also due to manufacturing tolerances there may be a little drift of the internal oscillators of the microcontrollers. Failure to synchronize could lead to changes in the current ripple. To see the possible phenomena, various simulations were carried out to see how component delays and drift could affect the ripple.

3.2.1 Frequency Drift

The first simulation performed, serves to show the possible consequences of a drift in the working frequency of the converters on the system. For simplification, three ideal voltage generators with the same voltage were set up and three different working frequencies were set.

Simulation Parameters	
I_{ref}	100 A
I_{ref} frequency	1 Hz
V_{in1}	80V
V_{in2}	80 V
V_{in3}	80 V
V_{out}	100 V
f_{sw1}	10 kHz
f_{sw2}	9.99 kHz
f_{sw3}	10.01 kHz
L	5.83 mH
ω_i	$1000 \cdot 2\pi\ rad/s$
K_p	$w_b \cdot L$
K_i	$0.2 w_b \cdot K_p$

Table 3.2: Parameters Value for Bidirectional DC-DC Converter's Simulation with frequency drift.

In Fig. 3.8 the current trend is shown, the frequency drift will not affect the whole system but only the amplitude of the current ripple. In this simulation the current ripple is affected by the phase shift of the commands of the various voltage generators.

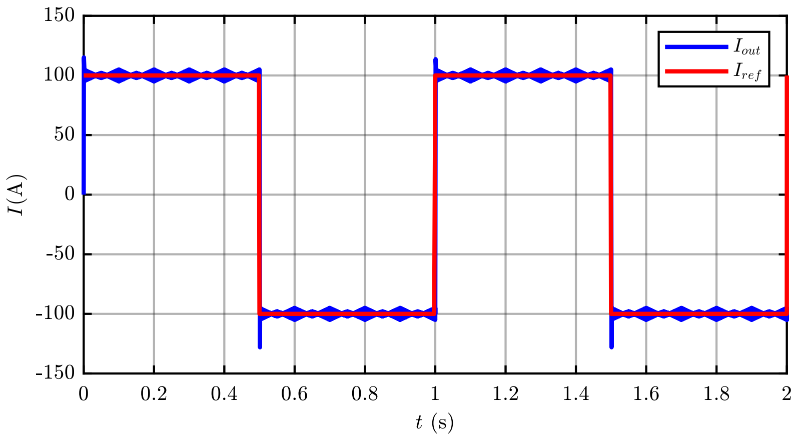

Figure 3.8: Current waveform with voltage frequency drift.

If we zoom in on the first quarter simulation as shown in Fig. 3.9, the ripple varies with a frequency of:

$$max(f_{sw1}, f_{sw2}, f_{sw3}) - min(f_{sw1}, f_{sw2}, f_{sw3}) = 20Hz \tag{3.5}$$

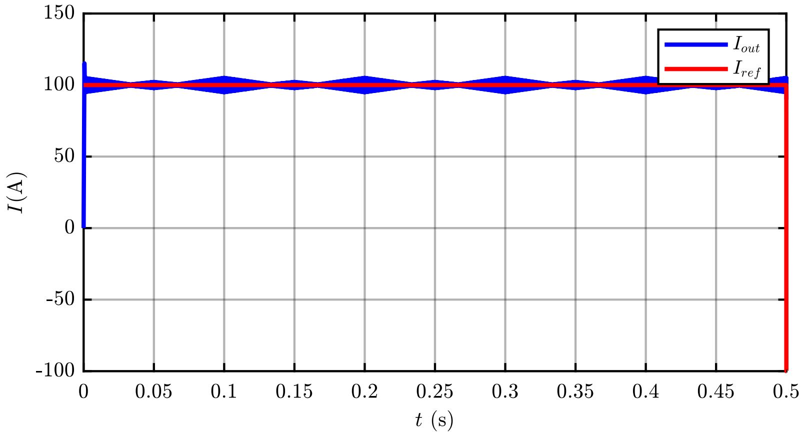

Figure 3.9: Frequency of Current Ripple.

3.2.2 Phase Shifting

The ripple will then be an alternating function dependent on the phase shift commands of the converters; it will, therefore, consist of an average value plus a superimposed phase shift-dependent ripple. It will, therefore, have a minimum and a maximum value. In order to investigate these values, further simulations were carried out. Considering three ideal voltage generators with the same voltage, several current step simulations were carried out by holding the carrier of the first converter stationary and varying the phase shift, oneleading and one in lagging the remaining two converters thus spanning the entire switching period and from time to time, when the current arrived at steady state, the amplitudes of the current ripples were saved and finally diagrammed with respect to the phase shifts of the carriers, the phase shift is written in per unit relative to the switching period $T_{sw} = 1/f_{sw}$.

Simulation Parameters	
I_{ref}	100 A
V_{in1}	80V
V_{in2}	80 V
V_{in3}	80 V
V_{out}	100 V
f_{sw}	10 kHz
$\Delta\phi_2$	0.05 pu
$\Delta\phi_3$	0.05 pu
L	5.83 mH
ω_i	$1000 \cdot 2\pi\ rad/s$
K_p	$w_b \cdot L$
K_i	$0.2 w_b \cdot K_p$

Table 3.3: Parameters Value for Bidirectional DC-DC Converter's Simulation with phase shifting.

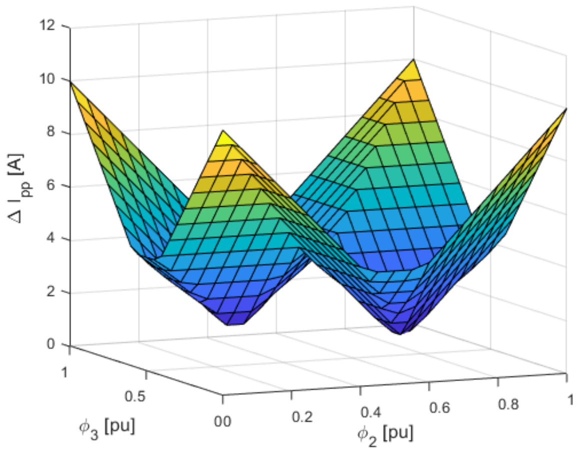

Figure 3.10: Current ripple variation for various phase shift.

It can be seen from the graphs in Fig. 3.10, Fig. 3.11a and in Fig. 3.11b that the ripple peaks occur when the three carriers are in phase with each other, that is, in the corners of the graph. Seeing the graph from above shown in Fig. 3.12, the minimum

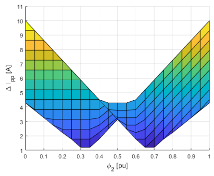

(a) Current ripple variation with respect to the second converter.

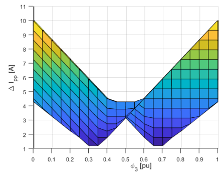

(b) Current ripple variation with respect to the third converter.

Figure 3.11: Current Ripple graphs

points of current ripple, the dark blue areas, occur in these intervals:

$$(\phi_2, \phi_3) = (0.30 - 0.35, 0.65 - 0.70) \tag{3.6}$$

$$(\phi_2, \phi_3) = (0.65 - 0.70, 0.30 - 0.35) \tag{3.7}$$

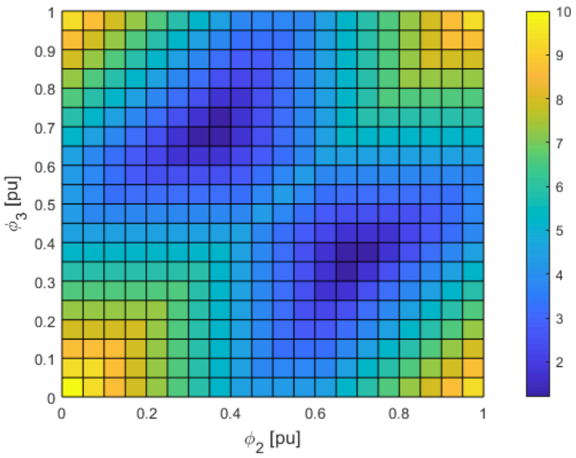

Figure 3.12: Current ripple cromatic diagram.

In the chromatic diagram, the points of minimum happen in the when the three carriers are equidistant from each other, in this case shifted $T_{sw}/3$ from each other. This phenomenon can be explained through an analysis to the harmonics of the system.

Analyze the phenomenon through a simplified system, assuming that the current control works properly. Consider the system shown in Fig. 3.13

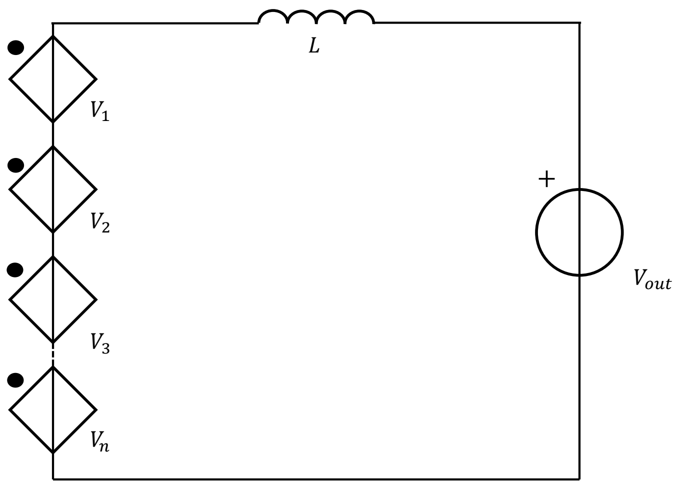

Figure 3.13: Simplified system with voltage-driven generators.

Consisting on

- m voltage-driven generators;
- Inductance L;
- DC voltage generator as output.

For simplicity, let us assume that the n voltage-driven generators generate rectangular pulse trains with frequency equal to f_{sw}, which are equal to each other and are out of phase with each other by t_{sw}/m. The generic equation written in fourier series of driven voltage generators will be as follows:

$$V_i = |V_i|\, d_i + \frac{2\,|V_i|}{\pi} \sum_{n=1}^{\infty} \frac{1}{n} \sin(\pi n d_i) cos(n\omega t + 2\pi n \frac{i}{m}) \tag{3.8}$$

Where $|V_i|$ is the amplitude of the rectangular wave and $\omega = 2\pi f_{sw}$ is the pulsation and n is the harmonic order. The equations of the system is as follows:

$$V_L = \sum_{i=1}^{m} V_i - V_{out} \tag{3.9}$$

$$V_L = L\frac{dI_L}{dt} \tag{3.10}$$

Under steady state conditions, the sum of the continuous components of the various generators will be equal to V_{out}, it follows that only the alternating components remain in the equation (3.9), it will became:

$$V_L = \sum_{i=1}^{m} \frac{2\,|V_i|}{\pi} \sum_{n=1}^{\infty} \frac{1}{n} \sin(\pi n d_i) cos(n\omega t + 2\pi n \frac{i}{m}) \tag{3.11}$$

Consequently, the current in the inductance will be as follows:

$$I_L = \frac{1}{L} \int \sum_{i=1}^{m} \frac{2\,|V_i|}{\pi} \sum_{n=1}^{\infty} \frac{1}{n} \sin(\pi n d_i) cos(n\omega t + 2\pi n \frac{i}{m}) \tag{3.12}$$

Due to the linearity property of the integral, we can exchange the sign of integral and summation

$$I_L = \frac{1}{L} \sum_{i=1}^{m} \frac{2\,|V_i|}{\pi} \sum_{n=1}^{\infty} \int \frac{1}{n} \sin(\pi n d_i) cos(n\omega t + 2\pi n \frac{i}{m}) \tag{3.13}$$

The Fourier series of the current in the inductance will be:

$$I_L = \frac{1}{L} \sum_{i=1}^{m} \frac{2\,|V_i|}{\pi} \sum_{n=1}^{\infty} \frac{1}{n^2\omega} \sin(\pi n d_i) \sin(n\omega t + 2\pi n \frac{i}{m}) \tag{3.14}$$

Let us now reduce the generic system by considering only three driven generators and we go on to perform a harmonic analysis of the system.

The system parameters will be the same as in the simulations and they are listed in Table 3.4 :

System Parameters	
I_{ref}	100 A
m	3
$\|V_1\|$	80V
$\|V_2\|$	80 V
$\|V_3\|$	80 V
V_{out}	100 V
f_{sw}	10 kHz
L	5.83 mH
ω_i	$1000 \cdot 2\pi\ rad/s$

Table 3.4: System parameters with driven generators

The remaining parameters can be calculated accordingly:

$$d_{avg} = \frac{V_{out}}{\sum_{i=1}^{3} |V_i|} = 0.4167 \tag{3.15}$$

$$d_i = n * d_{avg} \frac{|V_i|}{\sum_{i=1}^{3} |V_i|} = 0.4167 \tag{3.16}$$

The three voltages supplied by the generators will be as the following:

$$V_1 = |V_1|\, d_1 + \frac{2\,|V_1|}{\pi} \sum_{n=1}^{\infty} \frac{1}{n} \sin(\pi n d_1) cos(n\omega t + 2\pi n \frac{1}{3}) \tag{3.17}$$

$$V_2 = |V_2|\, d_2 + \frac{2\,|V_2|}{\pi} \sum_{n=1}^{\infty} \frac{1}{n} \sin(\pi n d_2) cos(n\omega t + 2\pi n \frac{2}{3}) \tag{3.18}$$

$$V_3 = |V_3|\, d_3 + \frac{2\,|V_3|}{\pi} \sum_{n=1}^{\infty} \frac{1}{n} \sin(\pi n d_3) cos(n\omega t + 2\pi n \frac{3}{3}) \tag{3.19}$$

If we replace (3.17), (3.18), (3.19) in (3.9) and simplify the dc components with V_{out}, we will get:

$$\begin{aligned} V_L = & \frac{2\left|V_1\right|}{\pi} \sum_{n=1}^{\infty} \frac{1}{n} \sin(\pi n d_1) cos(n\omega t + 2\pi n \frac{1}{3}) \\ & + \frac{2\left|V_2\right|}{\pi} \sum_{n=1}^{\infty} \frac{1}{n} \sin(\pi n d_2) cos(n\omega t + 2\pi n \frac{2}{3}) \\ & + \frac{2\left|V_3\right|}{\pi} \sum_{n=1}^{\infty} \frac{1}{n} \sin(\pi n d_3) cos(n\omega t + 2\pi n \frac{3}{3}) \end{aligned} \tag{3.20}$$

In Fig.3.14, the three separate components V_1, V_2, V_3 that forming V_L are shown, and in Fig.3.15 V_L is shown. The three voltages be perfectly equal to each other but only phase-shifted by $T_sw/3$ between them. The fundamental frequency of the three voltages is equal to f_{sw}. In contrast, the fundamental frequency of V_L is equal to $3f_{sw}$.

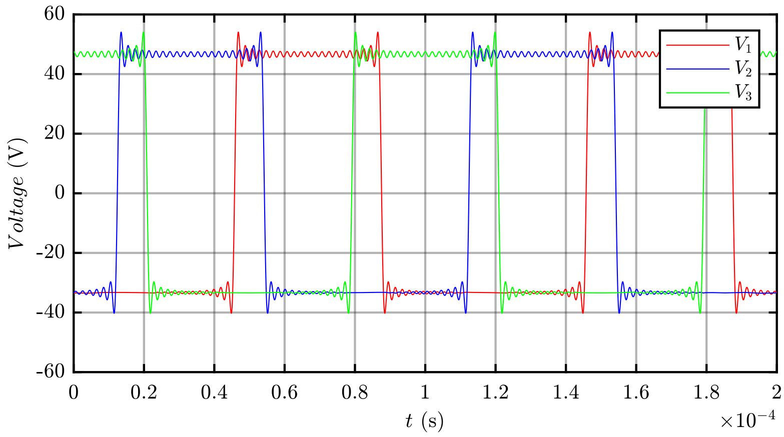

Figure 3.14: V_1, V_2 and V_3 in [0;2t_{sw}] with n = 50 .

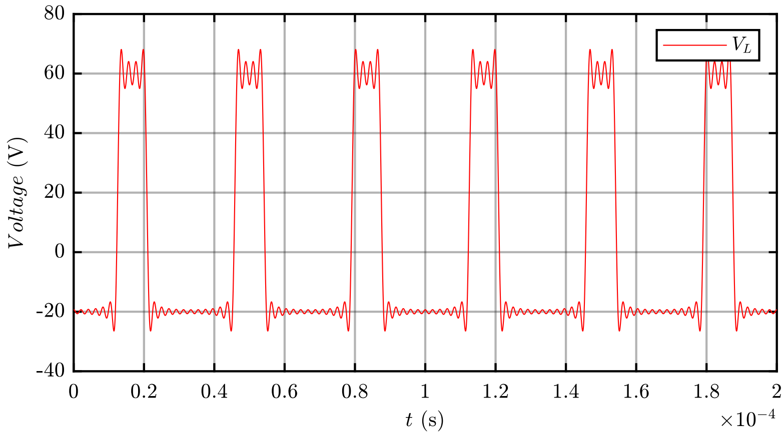

Figure 3.15: V_L in $[0;2T_{sw}]$ with $n = 50$.

Analyzing the equation in the various harmonic orders taken individually, Fig. 3.16 shows the first voltage harmonics of V_1, V_2 and V_3. Due to the initial phase shift, they will form a three-phase symmetrical system. In Fig. 3.17 the second-order harmonics of the three voltages are shown, again the initial phase shift will cause the formation of a three-phase symmetrical system.

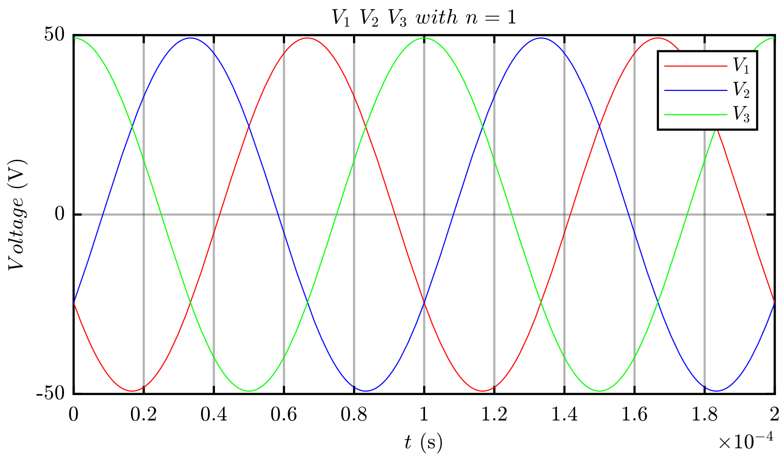

Figure 3.16: V_1, V_2 and V_3 in $[0;2t_{sw}]$ with $n = 1$.

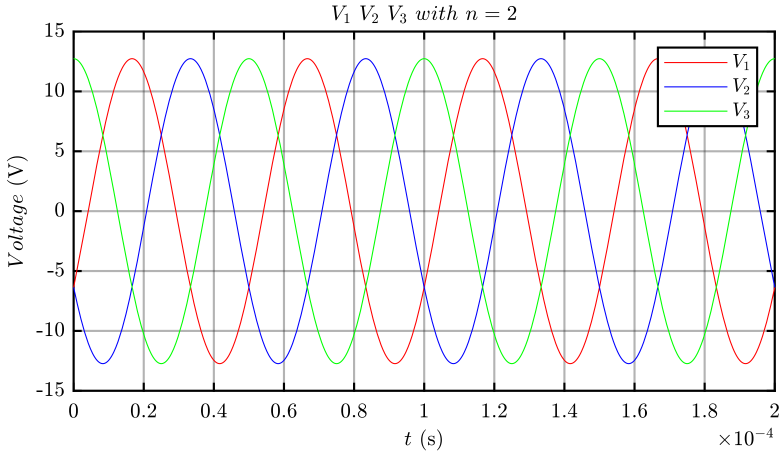

Figure 3.17: V_1, V_2 and V_3 in $[0;2t_{sw}]$ with $n = 2$.

If we analyze the third-order harmonic, this symmetry phenomenon does not occur; on the contrary, the harmonics in this case overlap perfectly. The three waveforms are shown in Fig.3.18.

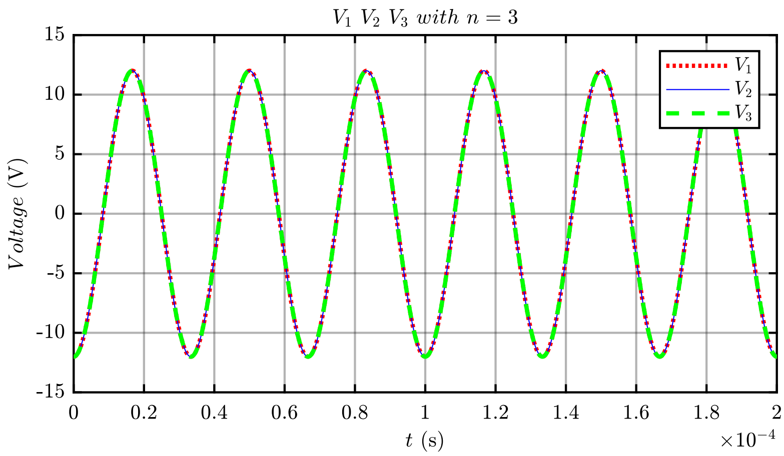

Figure 3.18: V_1, V_2 and V_3 in $[0;2t_{sw}]$ with $n = 3$.

This phenomenon due to the initial phase shift can also be seen with the fourth and fifth harmonics of the system, respectively in Fig. 3.19 and Fig. 3.20. Instead, in Fig.3.21 the system at the sixth harmonic is shown, as in the case of the third harmonic, the voltages will overlap each other.

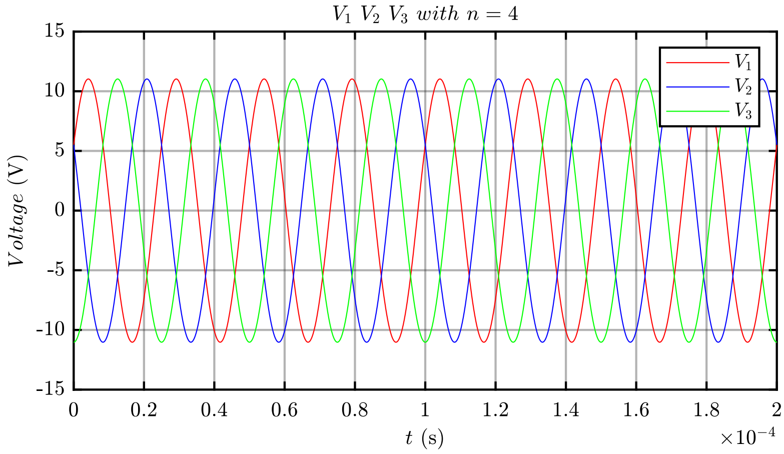

Figure 3.19: V_1, V_2 and V_3 in $[0;2t_{sw}]$ with $n = 4$.

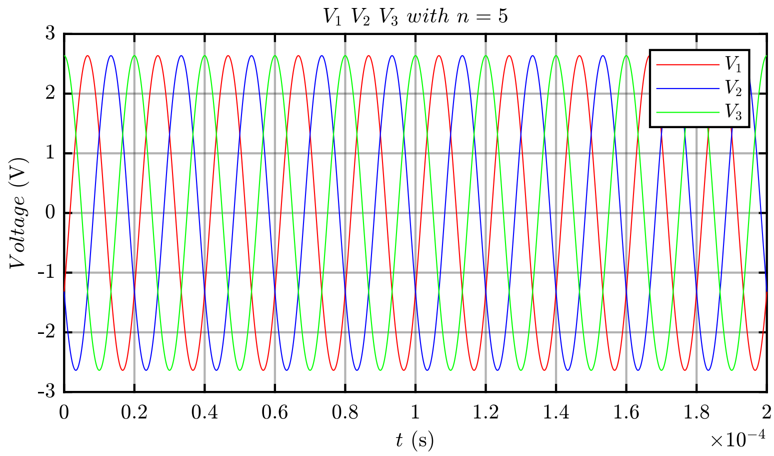

Figure 3.20: V_1, V_2 and V_3 in $[0;2t_{sw}]$ with $n = 5$.

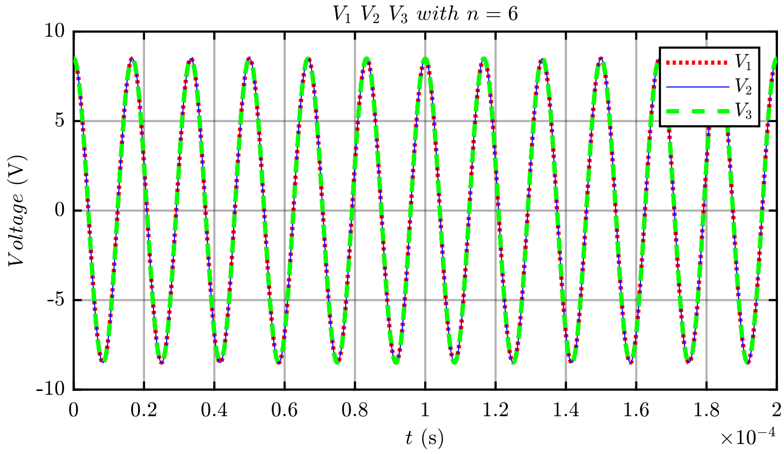

Figure 3.21: V_1, V_2 and V_3 in $[0;2t_{sw}]$ with $n = 6$.

This phenomenon caused by the initial phase shift leads to the formation of three-phase simmetrical system of all harmonic orders other than $n = km$ with $k = 1,2, \ldots\infty$. Symmetrical three-phase systems always having zero sum will not affect the current on the inductance, and the integral operator will not change this phenomenon in fact it only causes a delayed translation of the waveforms of the whole system while maintaining its symmetry. Consequently, all harmonic orders other than km can be removed from the (3.20). and it becames:

$$
\begin{aligned}
V_L = & \frac{2\,|V_1|}{\pi} \sum_{n=km}^{\infty} \frac{1}{n} \sin(\pi n d_1) cos(n\omega t + 2\pi n \frac{1}{3}) \\
& + \frac{2\,|V_2|}{\pi} \sum_{n=km}^{\infty} \frac{1}{n} \sin(\pi n d_2) cos(n\omega t + 2\pi n \frac{2}{3}) \\
& + \frac{2\,|V_3|}{\pi} \sum_{n=km}^{\infty} \frac{1}{n} \sin(\pi n d_3) cos(n\omega t + 2\pi n \frac{3}{3}) \\
& \qquad\qquad\qquad\qquad k = 1,2\ldots.\infty
\end{aligned}
\tag{3.21}
$$

The current in the inductance will then be:

$$
\begin{aligned}
I_L = {} & \frac{2\,|V_1|}{\pi L} \sum_{n=km}^{\infty} \int \frac{1}{n} \sin(\pi n d_1) \cos(n\omega t + 2\pi n \frac{1}{3}) \\
& + \frac{2\,|V_2|}{\pi L} \sum_{n=km}^{\infty} \int \frac{1}{n} \sin(\pi n d_2) \cos(n\omega t + 2\pi n \frac{2}{3}) \\
& + \frac{2\,|V_3|}{\pi L} \sum_{n=km}^{\infty} \int \frac{1}{n} \sin(\pi n d_3) \cos(n\omega t + 2\pi n \frac{3}{3})
\end{aligned}
\tag{3.22}
$$

Taking the integral out of (3.22), it becomes accordingly:

$$
\begin{aligned}
I_L = {} & \frac{2\,|V_1|}{\pi L} \sum_{n=km}^{\infty} \frac{1}{n^2\omega} \sin(\pi n d_1) \sin(n\omega t + 2\pi n \frac{1}{3}) \\
& + \frac{2\,|V_2|}{\pi L} \sum_{n=km}^{\infty} \frac{1}{n^2\omega} \sin(\pi n d_2) \sin(n\omega t + 2\pi n \frac{2}{3}) \\
& + \frac{2\,|V_3|}{\pi L} \sum_{n=km}^{\infty} \frac{1}{n^2\omega} \sin(\pi n d_3) \sin(n\omega t + 2\pi n \frac{3}{3})
\end{aligned}
\tag{3.23}
$$

Fig. 3.22 shows the comparison between the ripple in the inductance current first considering a phase shift between the voltage generators equal to T_{sw}/m and without phase shift. From the figures it can be seen that there is an increase in the frequency of the ripple and a consequent decrease in amplitude compared with the case without phase shift. This specific case can be extended to higher values of m, where all voltage harmonics other than $n = mk$ with $k = 1,2...\infty$ are eliminated, thus leading to an increase in the fundamental frequency of the ripple by a factor of m and a decrease in its amplitude. By phase-shifting the carriers it is then possible, for the same desired ripple amplitude, to decrease the inductance value by a factor m,obviously being careful with the current control parameters k_{pi} and k_{ii}.

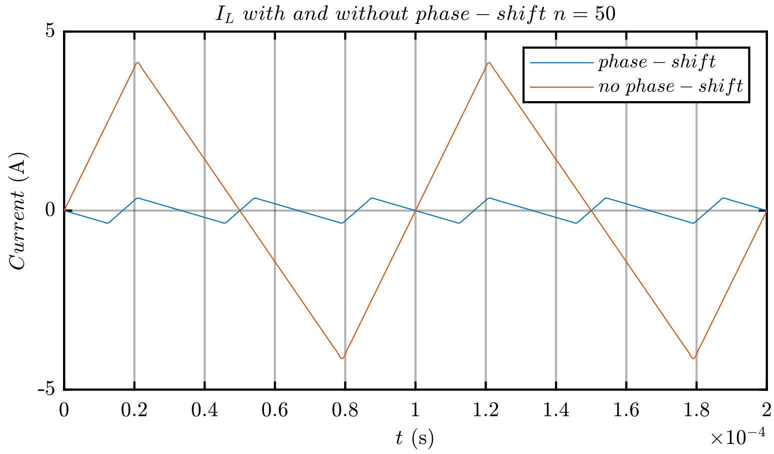

Figure 3.22: I_L with and without phase-shift in $[0;2t_{sw}]$ with $n = 50$.

This type of control also called PS-PWM [9] (phase-shifted PWM), used in many applications, leads to a reduction in ripple and a possible reduction in inductance. it is possible to implement it in a distributed system where each individual module has its own microcontroller, where a phase-shifted carrier is generated in each of them, the phase shift is calculated based on the number of active modules and assigned to the local controllers as soon as the system is activated. However, because of possible frequency drift as explained above, it is necessary for the master controller to send a synchronization signal every certain time interval so that the system is synchronized[8].

Chapter 4

Battery Control Implementation

This Chapter shows some specific system control methods by considering this time instead of ideal voltage generators real battery models as presented in the previous Chapter.

4.1 Battery Weights Factor Implementation

The implemented control strategy involves the division of power in the distributed system. This type of control is very often used in PV systems with the use of MPPTs. However, this strategy must have different characteristics than that of PV systems, our strategy must allow bidirectionality of power as opposed to PV systems, the criterion by which power is distributed in our system must depend on various parameters of individual modules such as voltage, capacitance, not like PV systems that depend only on irradiation conditions. The control system implemented will be based on weight factors, which will go to represent the "status" of each individual module, so as to ensure an adequate discharge cycle of the various modules [6]. Thus, the control strategy will have to ensure the following:

$$\frac{I_{batt,1}}{\omega_1} = \frac{I_{batt,2}}{\omega_2} = \ldots = \frac{I_{batt,n}}{\omega_n} \tag{4.1}$$

The values of these weights can be very different from each other since we may have modules with different capacities or SOCs from each other. The main objective of the control is to ensure proper current control through average duty and to properly control the various modules with the right weights to make the best use of them. One possible method of implementing the weights can be derived from the fundamental battery charge/discharge equation. The fundamental charge equation for a battery module is given by (4.2) where $SOC_{\%0}$ is the initial percentage charged stored.

$$SOC_{\%}(t) = SOC_{\%0} + \frac{100}{C \cdot T} \int_0^T i_{batt} dt = f(OCV(t)) \tag{4.2}$$

Where C is the battery capacity in Ah and $T = 3600s$ in order to convert the value from datasheet in a percentage value. Now assuming that the charge in the battery is some function of the open-circuit voltage:

$$f(OCV(t)) = f(OCV_0(t)) + \frac{100}{C \cdot T} \int_0^T i_{batt} dt \tag{4.3}$$

where the OCV_0 is the voltage measured at the initial instant, It will indicate the initial SOC. Assuming a time $T_{min/max}$ for the duration of the charge/discharge process by which it must end. Therefore:

$$OCV(T_{min/max}) = OCVmin/max \tag{4.4}$$

Where $OCVmin/max$ is the module maximum or minimum OCV at time $T_{min/max}$. Under this condition (4.3) becomes

$$f(OCV_{min/max}) = f(OCV_0) + \frac{100}{C \cdot T}\int_0^{T_{min/max}} i_{batt}dt \tag{4.5}$$

From (4.5) the charge/discharge current,

$$\int_0^{T_{min/max}} i_{batt}dt = \frac{CT}{100}\left(f(OCV_{min/max}) - f(OCV_0)\right) \tag{4.6}$$

This equation (4.6) can be solved by assuming the following approximation:

$$I_{batt} \approx \frac{CT}{100}\left(\frac{f(OCV_{min/max}) - f(OCV_0)}{T_{min/max}}\right) \tag{4.7}$$

where I_{batt} is the magnitude of the charging/discharging current. This assumption is accurate if the minimum battery voltage of a module is higher than the change in battery voltage range between fully charged to discharged, otherwise, inaccuracies may be introduced. $OCV_{min/max}$ should be known for a particular model based precharacterization. $T_{min/max}$ will be common across all the modules as they are to be charged at the same time. However, in a lots of application, $T_{min/max}$ will be unknown. To eliminate $T_{min/max}$ from (4.7), the converter power balance equation can be used as shown in (4.8):

$$P = \sum_{k=1}^{n} V_{batt,k} I_{batt,k} \tag{4.8}$$

Where n is the number of active modules, and each module k has a different voltage $V_{batt,k}$ and current $I_{batt,k}$. Now, substituting (4.7) into (4.8) for each module k gives

$$P = \sum_{k=1}^{n} V_{batt,k}\frac{C_k T}{100}\left(\frac{f(OCV_{min/max,k}) - f(OCV_{0,k})}{T_{min/max}}\right) \tag{4.9}$$

To find, for example, $I_{batt,1}$, and eliminate $T_{min/max}$ from (4.9), which is equal for all modules, substitute for $T_{min/max}$ from (4.7),

$$P = \sum_{k=1}^{n} V_{batt,k} \frac{C_k}{C_1} \frac{f(OCV_{min/max,k}) - f(OCV_{0,k})}{\left(\frac{f(OCV_{min/max,1}) - f(OCV_{0,1})}{I_{batt,1}}\right)} \tag{4.10}$$

Rearranging (4.10) gives the desired module battery current:

$$I_{batt,1} = P \cdot \left(\frac{C_1 \cdot \left(f(OCV_{min/max,1}) - f(OCV_{0,1})\right)}{\sum_{k=1}^{n} V_{batt,k} C_k \left(f(OCV_{min/max,k}) - f(OCV_{0,k})\right)} \right) \tag{4.11}$$

Therefore, the generic battery current $I_{batt,i}$ can be written as follows:

$$I_{batt,i} = P \cdot \left(\frac{C_i \cdot \left(f(OCV_{min/max,i}) - f(OCV_{0,i})\right)}{\sum_{k=1}^{n} V_{batt,k} C_k \left(f(OCV_{min/max,k}) - f(OCV_{0,k})\right)} \right) = P \cdot \omega_i \tag{4.12}$$

Because of the implemented LUT we know the relationship between SOC and OCV, it is then possible to rewrite (4.12) in terms of the $SOC_{\%}$:

$$I_{batt,i} = P \cdot \left(\frac{C_i \cdot \left(SOC_{\% min/max,i} - SOC_{\% 0,i}\right)}{\sum_{k=1}^{n} V_{batt,k} C_k \left(SOC_{\% min/max,k} - SOC_{\% 0,k}\right)} \right) = P \cdot \omega_i \tag{4.13}$$

Considering separately the cases of charging and discharging, for charging the weights will be as follows:

$$\omega_i = \frac{C_i \cdot \left(SOC_{\ max,i} - SOC_{\% 0,i}\right)}{\sum_{k=1}^{n} V_{batt,k} C_k \left(SOC_{\% max,k} - SOC_{\% 0,k}\right)} \tag{4.14}$$

Instead, for discharging:

$$\omega_i = \frac{C_i \cdot \left(SOC_{\% 0,i} - SOC_{\ min,i}\right)}{\sum_{k=1}^{n} V_{batt,k} C_k \left(SOC_{\% 0,k} - SOC_{\% min,k}\right)} \tag{4.15}$$

Taking (3.4) again, to have duties proportional to the weights just calculated, the formula will change accordingly:

$$d_i = n \cdot d_{avg} \cdot \frac{\omega_i \cdot V_{in,i}}{\sum_{i=1}^{n} \omega_i V_{in,i}} \tag{4.16}$$

4.1.1 Simulation of a Real Module String

Consider three modules consisting of three identical real battery packs and three converters, the model of the generic battery cell implemented is shown in Fig. 4.1

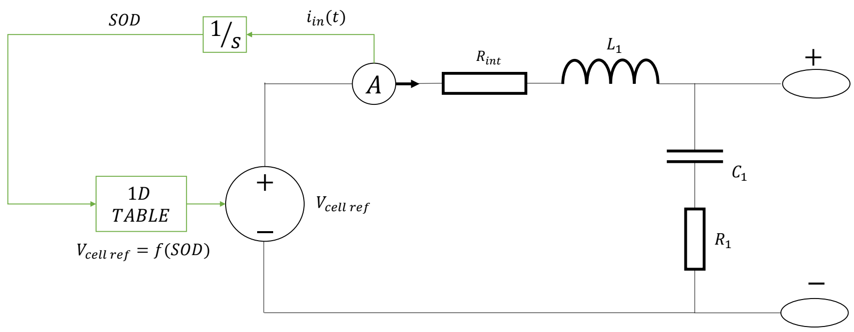

Figure 4.1: Real Battery Model Implemented.

In the new model L_1 represents the system leakage inductance between cables, busbars, and battery connections, and C_1 and R_2 are parameters proper to dc-dc converters. For these simulations, some model parameters are not representative of an existing real system but have been set ad hoc in order to show how the control algorithm works, significant variations in SOC and other quantities.

Simulation Parameters	
I_{ref}	100 A
I_{ref} frequency	1 Hz
$I_{ref}\ duty$	0.8
V_{cell}	4.1 V
n_s	20
n_p	0.01
L_1	2µH
C_1	670 µF
R_2	1m Ω
L	5 mH
V_{out}	100 V
f_{sw}	10 kHz
L	5 mH
ω_i	$1000 \cdot 2\pi\ rad/s$
K_p	$w_b \cdot L$
K_i	$0.2 \cdot w_b \cdot K_p$

Table 4.1: Parameters Value for Real String Batteries Simulation

The current trend is shown in Fig. 4.2 which, as in previous cases, correctly follows the reference.

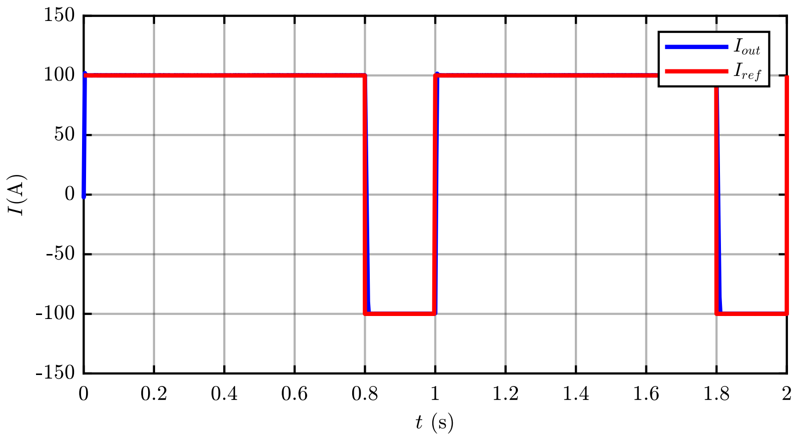

Figure 4.2: Current trend in a real battery string.

The most important quantities to see are the SOC trends, in Fig. 4.3, the trends are shown, equal to each other since the three modules are identical to each other and have same initial SOC.

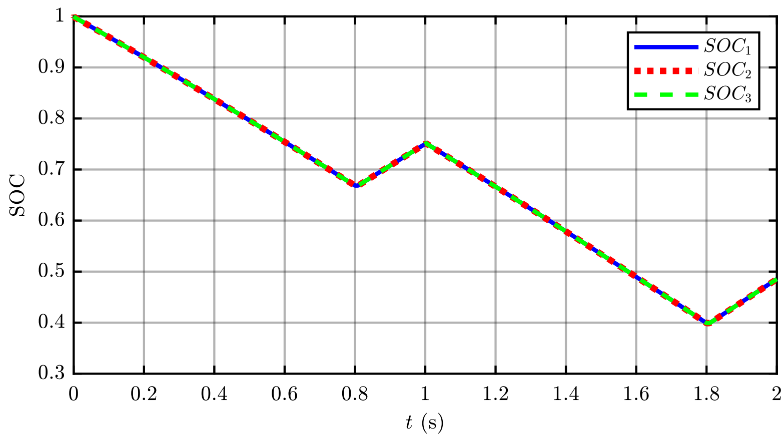

Figure 4.3: SOC trend in a real battery string.

Other simulations were carried out by going to change the initial SOC of the three different modules so as to verify the control performance and the various quantities. The initial SOCs of the various modules are shown in Table 4.2 The rest of the parameters are the same as in Table 4.4

Simulation Parameters	
SOC_1	100%
SOC_1	90%
SOC_3	80%

Table 4.2: Initial SOC for the Real Battery String.

Fig. 4.4 shows the current trend, which correctly follows the reference. The most significant trend to be displayed is the SOC of the various modules, shown in Fig. 4.5

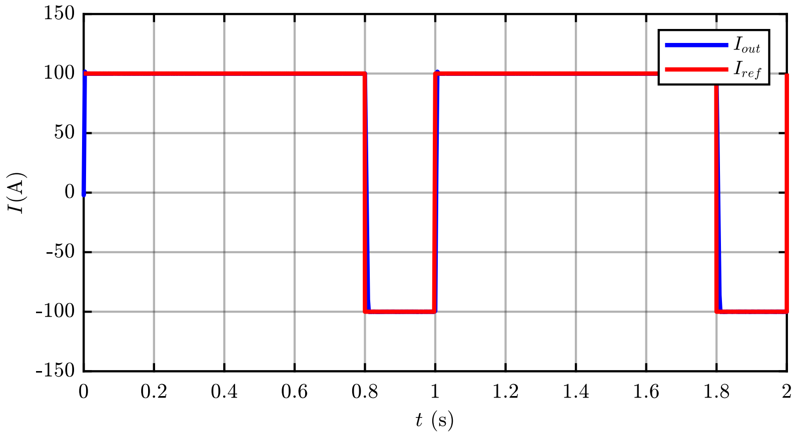

Figure 4.4: Current trend in a real battery string with different initial SOC.

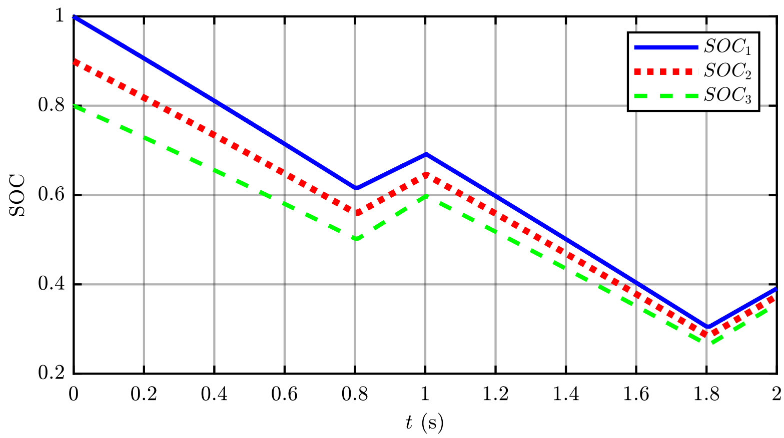

Figure 4.5: SOC trend in a real battery string with different initial SOC.

Starting from SOCs of 100%, 90% and 80% respectively at the end of the simulation after two different time processes of charge and discharge, the three modules reached charge levels of 39%, 37% and 36% respectively.The time is of simulation is deliberately short because of the high computational time and because the simulated system is a scaled system where we want to show the proper functioning of the implemented algorithm. The control has, therefore, generated appropriate ω_i weights to bring the batteries to the same conditions in order to exploit them equally. In Fig. 4.6 we can see the trend of the various

d_i throughout the simulation, which will vary over time to maintain the current reference and battery utilization according to the various ω_i. They will have a similar trend to the corresponding SOCs, in fact they will converge until they are equal.

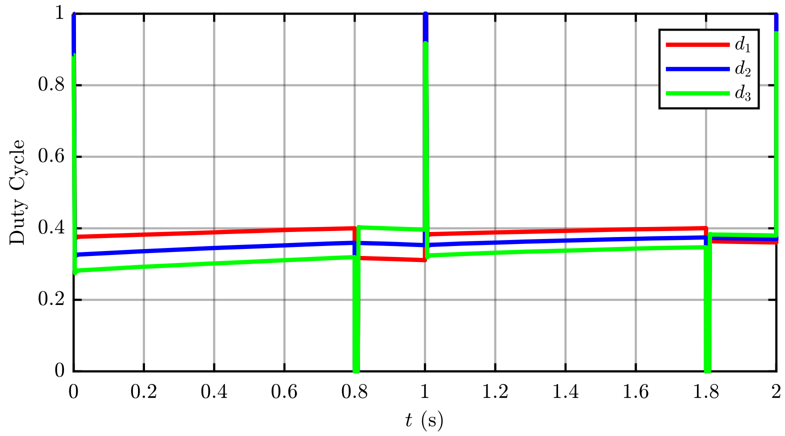

Figure 4.6: Duty Cycles trend in a real battery string with different initial SOC.

As described earlier in (4.16), if the system is working properly the following relationship is always valid

$$n \cdot d_{avg} = \sum_{i=1}^{n} d_i \tag{4.17}$$

It as seen in Fig. 4.7 is respected, the only instants in which we can notice differences is in the transients due to possible saturations of the system.

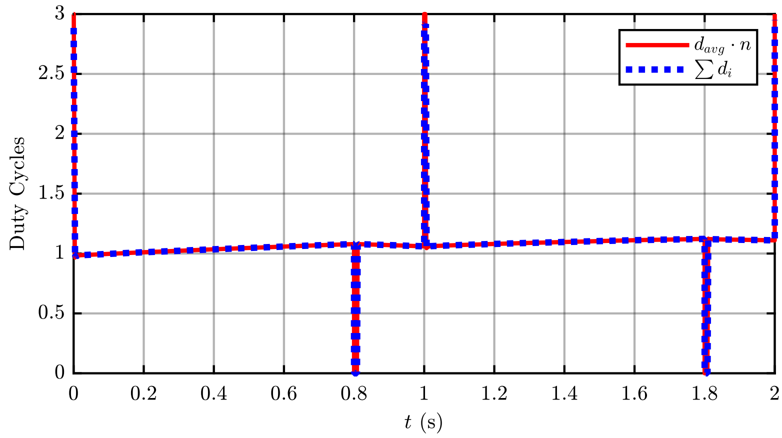

Figure 4.7: Relationship between d_{avg} and d_i.

As in the previous simulation, duties are compared with three carriers shifted from each other by $T_{sw}/3$, as shown in Fig. 4.8, and output voltages are generated accordingly.

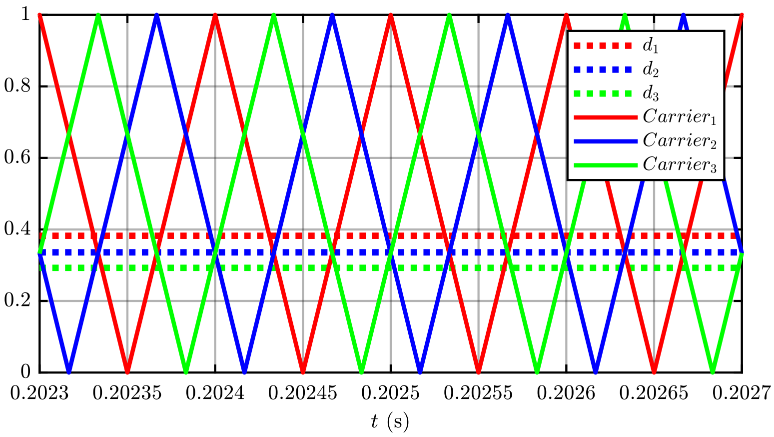

Figure 4.8: d_i with their Carrier.

4.2 SOC Balancing Controller

This section explains a different control method, which will monitor the state of charge of the batteries and try to bring them to the same level [10]. This control consists of two control loops, the first one adjusts the current and the second one adjusts the SOC. A block diagram of the control is shown in Fig. 4.9.

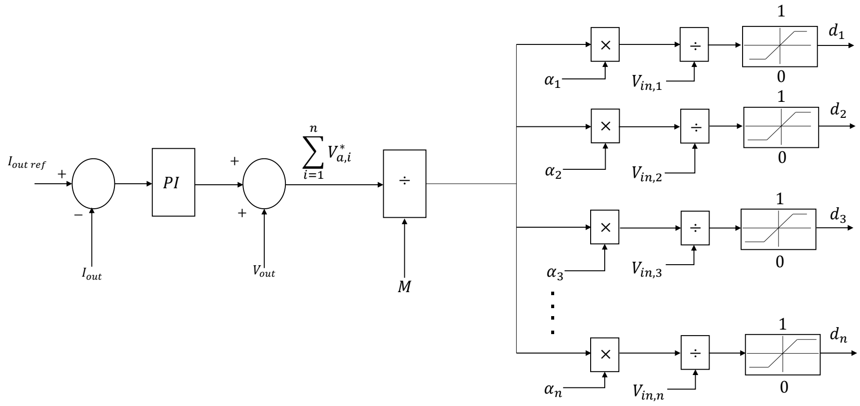

Figure 4.9: Current Control Loop for Balancing Control.

The output of the current control is divided by M :

Which is:

$$M = \sum_{i=1}^{N} \alpha_i \tag{4.18}$$

The sizing of the control loop is always the same as set in the previous chapters, through a PI controller. The output of the current loop is then divided into the various modules in order to adjust the output voltage of each module. We can therefore write that:

$$V_{a,i} = \frac{\sum_{i=1}^{n} V_{a,i}^{*}}{M} \cdot \alpha_i \tag{4.19}$$

The multipliers α_i are calculated within the second loop through comparison with a SOC_{ref}, as shown in Fig. 4.10.

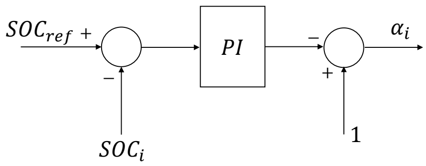

Figure 4.10: SOC Control Loop in discharge mode.

An offset equal to 1 is added to the output of the control so that the batteries start with the same exploitation. In addition, a saturator between 0 and 2 was added for the various α_i so that there are no problems on the control and still ensure equal utilization of the various modules. The various multipliers α_i are modified to control the discharge of the various modules so that the SOC of the various batteries can be controlled. The SOC of each module is compared with a reference value SOC_{ref} so as to keep the state of charge of each module balanced with each other. If the SOC_i is less or greater than the SOC_{ref}, it will go to affect the corresponding multiplier α_i. Since the output current for all modules is the same, the different output voltage values of the various modules will go to affect their discharge. This will continue until the SOC values are all balanced with each other. In case of reloading, the control will be the same but with the modification of some marks in the control, as shown in Fig. 4.11

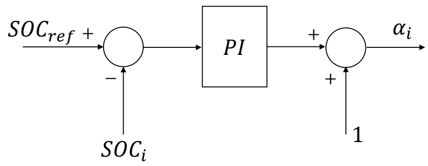

Figure 4.11: SOC Control Loop in charge mode.

The value of SOC_{ref} is nothing but the average of the various SOC_i of the various modules.

$$SOC_{ref} = \frac{\sum_{i=1}^{n} SOC_i}{n} \tag{4.20}$$

The sizing of the second loop must take into account several factors, it must in fact be slower than the current loop and the values of $k_{p,SOC}$ and $k_{i,SOC}$ must be such as to ensure a fast equalization of the charges without immediately saturating the system by arriving at a possible loss of current control.

4.2.1 Simulation of SOC Controller

To show how the system works, a simulation was implemented with the same parameters set for the previous control reported again below:

Simulation Parameters	
SOC_1	100%
SOC_2	90%
SOC_3	80%
I_{ref}	100 A
I_{ref} frequency	1 Hz
$I_{ref}\ duty$	0.8
V_{cell}	4.1 V
n_s	20
n_p	0.01
L_1	2μH
C_1	670 μF
R_2	1m Ω
L	5 mH
V_{out}	100 V
f_{sw}	10 kHz
L	5 mH
ω_i	$800 \cdot 2\pi\ rad/s$
$K_{p,i}$	$w_b L$
$K_{i,i}$	$0.1 \cdot w_b \cdot K_p$
ω_i	$10 \cdot 2\pi\ rad/s$
$k_{p,SOC}$	$0.1 \cdot \omega_b \cdot L$
$K_{i,i}$	0

Table 4.3: Parameters Value for Real String Batteries Simulation

Fig. 4.12 shows the current trend where it can be seen that it follows the reference perfectly. The most important quantity to look at is the SOC of of the three modules in Fig. 4.13

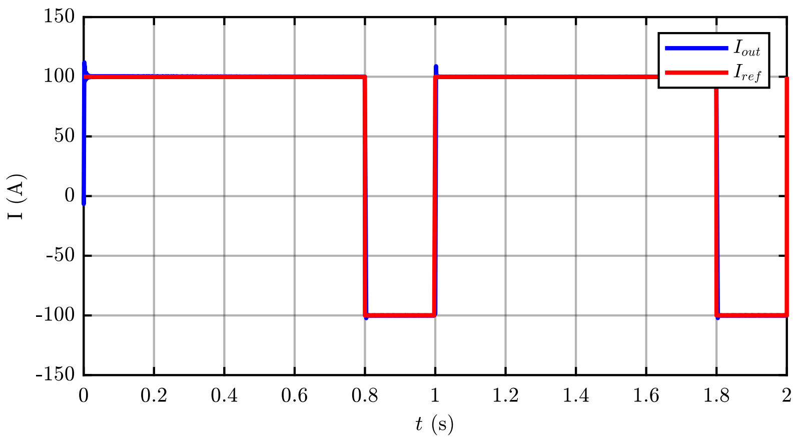

Figure 4.12: Current trend for SOC Balancing Controller.

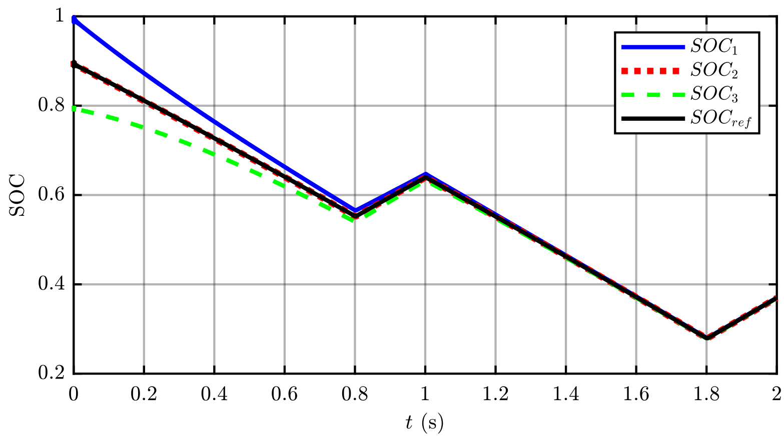

Figure 4.13: SOC trend for SOC Balancing Controller.

It can be seen that starting from different SOC values, at the end of the charge/discharge cycle the modules align with the same value of SOC_{ref}. Fig. 4.14 shows the trend of the error between different SOC_i with SOC_{ref}, as it can be guessed it will go toward zero.

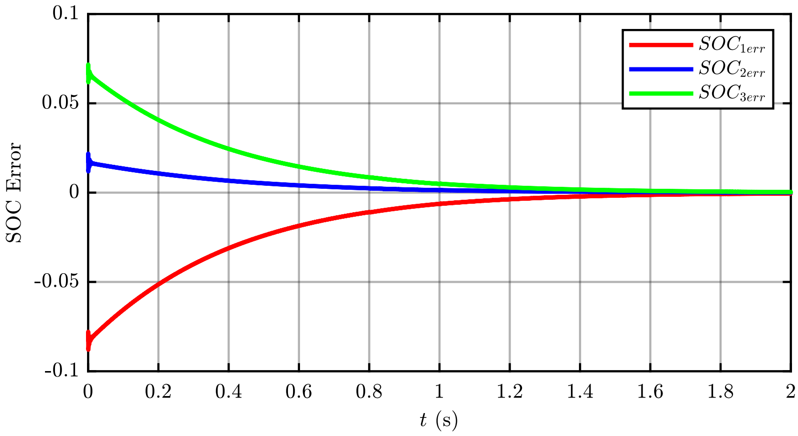

Figure 4.14: SOC_{err} trend for SOC Balancing Controller.

Finally, shows the trends of the weights, which converge to one and at each sign change of the current take on a value symmetrical to the offset implemented in the control.

4.2.2 Adaptive $K_{p,SOC}$

In order to properly size $k_{p,SOC}$ we carry out consider the following power balance. We consider the converters to be ideal, we can therefore write that:

$$V_{batt,i} \cdot I_{batt,i} = V_{a,i} \cdot I_{out} \tag{4.21}$$

Substituting (4.19) in (4.21)

$$V_{batt,i} \cdot I_{batt,i} = \frac{\sum_{i=1}^{n} V_{a,i}^{*}}{M} \cdot \alpha_i \cdot I_{out} \tag{4.22}$$

The battery current $I_{batt,i}$ can be written as follows:

$$I_{batt,i} = C \cdot \left(\frac{dSOC_i}{dt}\right) \tag{4.23}$$

Where C is the nominal capacity of the battery. By substituting (4.24) into (4.22), the following equation can be derived:

$$\frac{dSOC_i}{dt} = \alpha_i \cdot \left(\frac{\sum_{i=1}^{n} V_{a,i}^*}{M} \right) \cdot \frac{I_{out}}{C \cdot V_{batt,i}} \tag{4.24}$$

The block diagram of the control system will, therefore, be as follows:

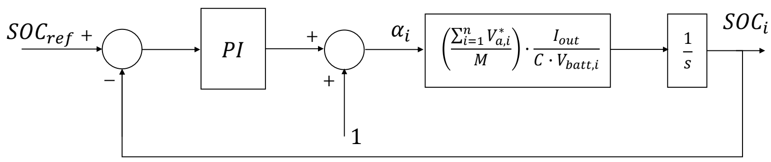

Figure 4.15: SOC Control Diagram.

The ideal value of $K_{p,SOC}$ is as follows:

$$k_{p,SOC} = \omega_{b,SOC} \cdot \left(\frac{M}{\sum_{i=1}^{n} V_{a,i}^*} \right) \cdot \frac{C \cdot V_{batt,i}}{I_{out}} \tag{4.25}$$

These parameters, however, are all time-varying, so we would need a time-varying $k_{p,SOC}$, i.e., adaptive. In order to evaluate the system performance, current step simulations were carried out with adaptive and non-adaptive $k_{p,SOC}$ at various current step values in order to evaluate their trends. To do this, a model had to be implemented at the average values of the system, thus neglecting the switching so that higher time intervals could be simulated with less computational power. For these simulations, the dc-dc converters are eliminated thus dividing the system into two separate circuits, one on the battery side and one on the load side. The battery-side circuit is as follows shown in Fig. 4.16

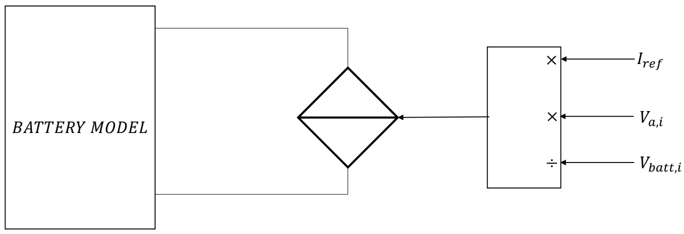

Figure 4.16: Average Battery Model.

On the load side, on the other hand, the system at average values is shown in Fig.4.17, consisting of voltage-driven generators that generate the output voltages of the current control loop, the inductance L and the voltage generator V_{out}.

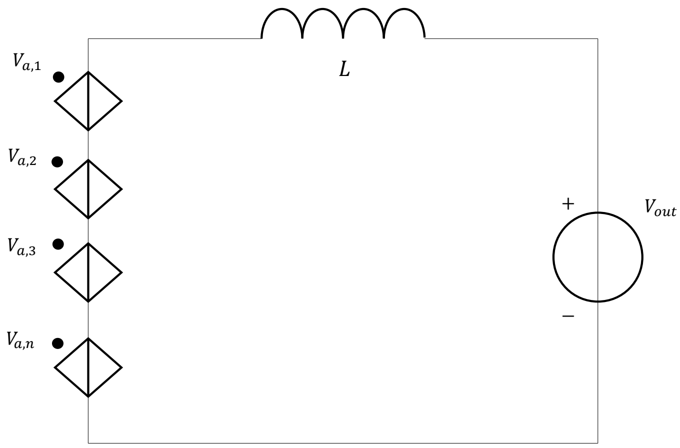

Figure 4.17: Average Model of the load side.

Simulations were performed at various current steps comparing the various $SOC_{err,i}$ in the adaptive and constant case, seeing the differences in the two case. In Table 4.4 are shown the parameters of the simulations

Simulation Parameters	
Simulation Time	250 s
SOC_1	100%
SOC_2	90%
SOC_3	85%
I_{ref} frequency	1/60 Hz
$I_{ref}\ duty$	0.5
V_{cell}	4.1 V
C	2.250 Ah
n_s	20
n_p	1
L	5 mH
V_{out}	100 V
L	5 mH
ω_i	$800 \cdot 2\pi\ rad/s$
$K_{p,i}$	$w_b L$
$K_{i,i}$	$0.1 w_b K_p$
ω_i	$10 \cdot 2\pi\ rad/s$

Table 4.4: Parameters Value for Real String Batteries Simulation

For each simulation, the non adaptive $k_{p,SOC}$ to be used in the simulation were calculated. The values of the parameters used and the graphs of $SOC_{i,err}$ compared as the reference current changes will be shown below.

Simulation Parameters	
I_{ref}	100
$k_{p,SOC1}$	22
$k_{p,SOC2}$	18
$k_{p,SOC2}$	15

Table 4.5: $K_{p,SOC}$ values for the Simulation with I_{ref}=100A.

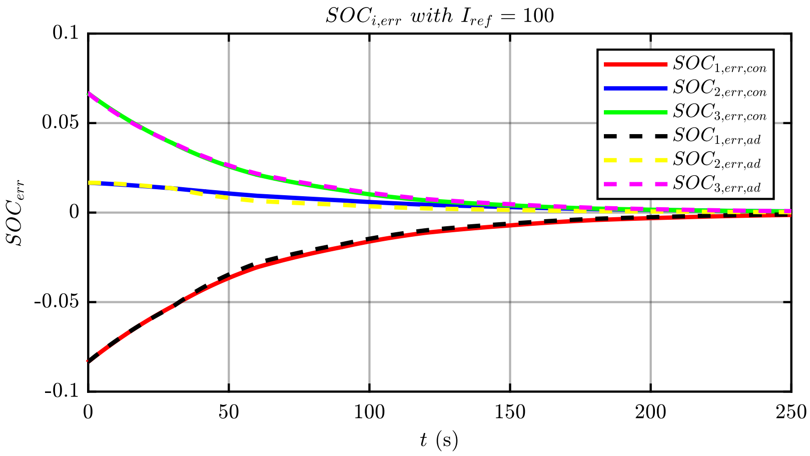

Figure 4.18: $SOC_{i,err}$ with $I_{ref} = 100A$.

Simulation Parameters	
I_{ref}	150
$k_{p,SOC1}$	31
$k_{p,SOC2}$	27
$k_{p,SOC2}$	23

Table 4.6: $K_{p,SOC}$ values for the Simulation with I_{ref}=150A.

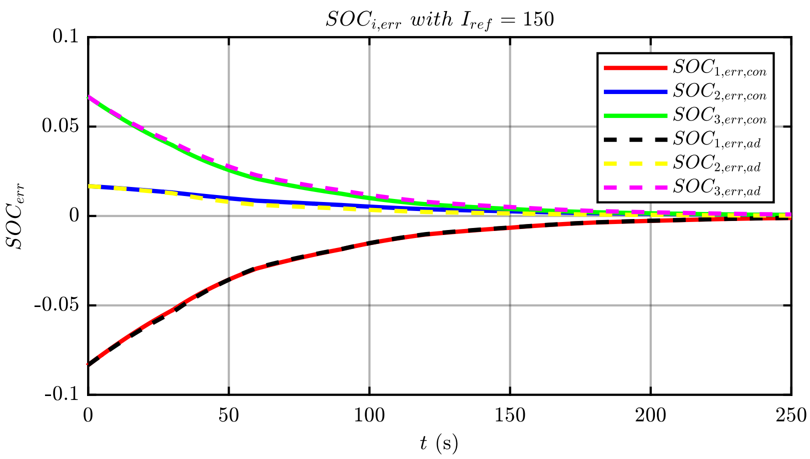

Figure 4.19: $SOC_{i,err}$ with $I_{ref} = 150A$.

Simulation Parameters	
I_{ref}	200
$k_{p,SOC1}$	40
$k_{p,SOC2}$	36
$k_{p,SOC2}$	33

Table 4.7: $K_{p,SOC}$ values for the Simulation with I_{ref}=200A.

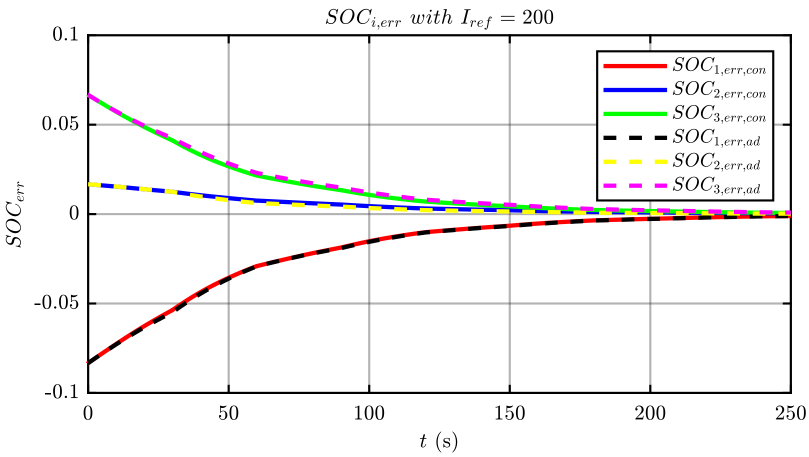

Figure 4.20: $SOC_{i,err}$ with $I_{ref} = 200A$.

Simulation Parameters	
I_{ref}	250
$k_{p,SOC1}$	49
$k_{p,SOC2}$	45
$k_{p,SOC2}$	42

Table 4.8: $K_{p,SOC}$ values for the Simulation with I_{ref}=250A.

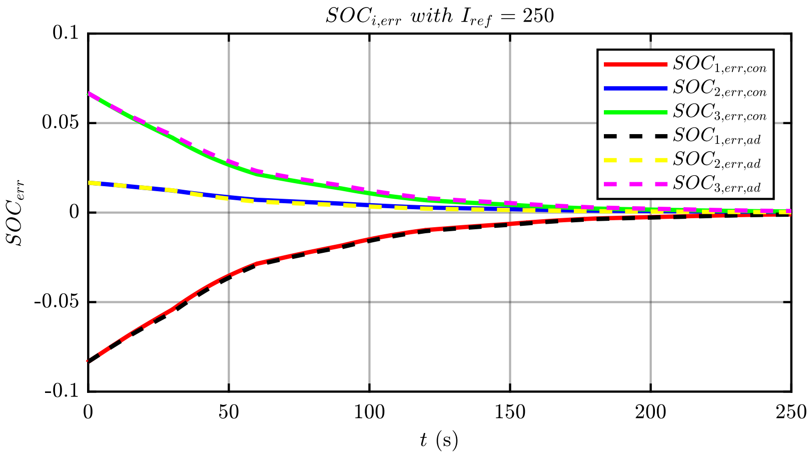

Figure 4.21: $SOC_{i,err}$ with $I_{ref} = 250A$.

It can be seen from the various grahps that the difference between the adaptive and constant cases is really minimal, the values of $k_{p,SOC,i}$ constants calculated at the beginning of the transient manage to give a good approximation of the trend of the adaptive case.

Chapter 5

Real Load Profile Simulation

In this Chapter, the response of the system to a real daily load of ships of various types and applications is seen through simulations at the average values of the first type of control implemented.

5.1 Average System Implementation

As in the previous simulation, digital control is abandoned for simulation at average values so that a real daily load simulation of various ship applications can be simulated without onerous computational cost. The system represented will, therefore, be divided into two separate circuits, one on the battery side and one on the load side.
On the battery side in this case three different cell types will be implemented, thus with different voltage curves and capacity values between them. As shown above, the circuit at the average values on the battery side is like that shown in Fig. 5.1

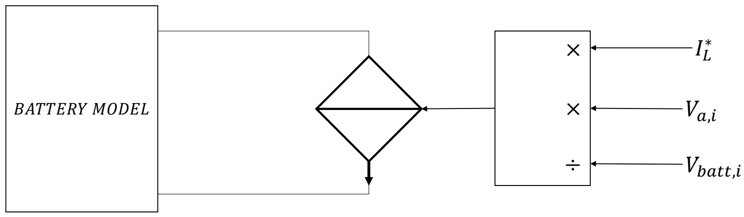

Figure 5.1: Average Battery Model for Real Application.

The purpose of the battery circuit model is, assuming that the current control works properly, to simulate the discharge and recharge of the modules so as to see how they behave to the demands of the simulated system. The ideal current generator will absorb the current required by the load multiplied by the duty cycle d_i coming from the current control. Fig. 5.2 shows the model implemented on the load side.

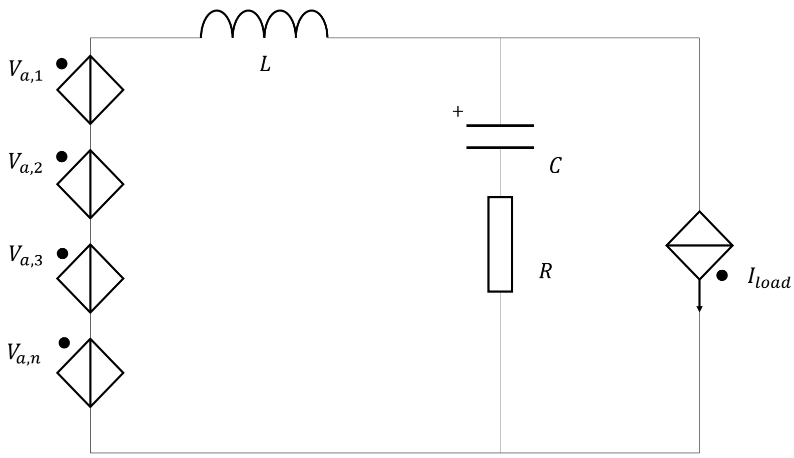

Figure 5.2: Average Model of the Load Side.

This average modell consists of several ideal voltage generators that will generate the voltages coming from the current control, a capacitance, a resistor, an inductance and a current generator that will generate the reference current from the diagram coming from a look up table.

5.1.1 Control Implementation

In this case, we will have two control loops implemented, an external voltage loop regarding the voltage on the capacitance and an internal voltage loop for the current on the inductance. In Fig.5.3 is shown the first loop.

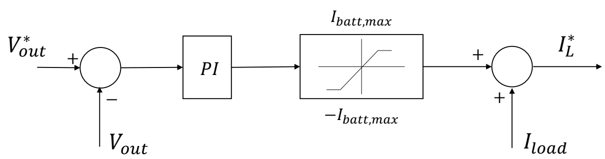

Figure 5.3: Voltage Loop Control.

The sizing of the voltage loop is very simple and standard; set the bandwidth of the lower loop to the current loop, the sizing of $k_{p,V}$ and $k_{i,V}$ is as follows:

$$\begin{cases} k_{p,V} = \omega_{b,V} \cdot C \\ k_{i,V} \ll k_{p,V} \cdot \omega_{b,V} \end{cases} \tag{5.1}$$

The internal current loop is shown in Fig.5.4; its dimensioning is the same as shown above and is as follows:

$$\begin{cases} k_{p,I} = \omega_{b,I} \cdot L \\ k_{i,I} \ll k_{p,I} \cdot \omega_{b,I} \end{cases} \tag{5.2}$$

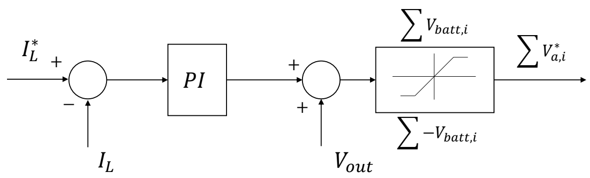

Figure 5.4: Current Loop Control.

From the output of the current control, the d_{avg} will then be calculated and through the calculation of the various weights d_i and consequently the voltages of the driven generators.

5.2 System Specification

The simulated system must represent a scaled-up real system. In a real system about ten modules will be implemented. For this simulation three modules of 400 V each with $V_{out}^* = 1000V$ are considered. The load diagrams are data taken from real diagrams, time vs power; an example is shown in Fig.5.5

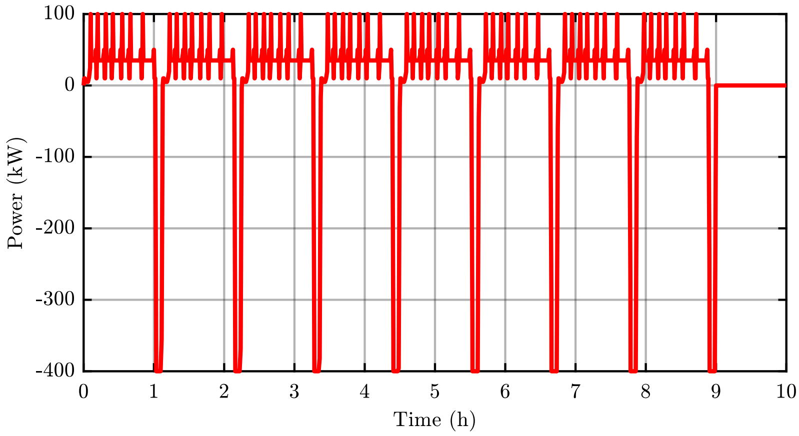

Figure 5.5: Example of Load Cycle.

Through the clok block and a look up table with the load diagram implemented, the output power will be calculated which then divided by the V^*_{out} will give me the output current of the voltage generator as shown in Fig. 5.6

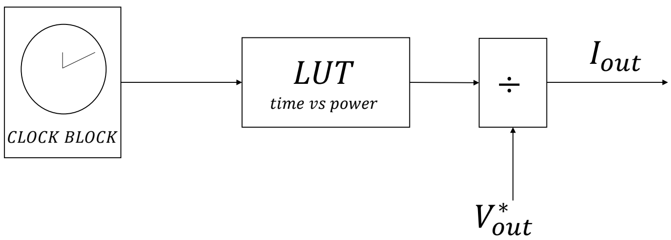

Figure 5.6: I_{out} Block Diagram

For the simulation, the model presented in the previous chapter was used, which is reproduced in Fig. 5.7

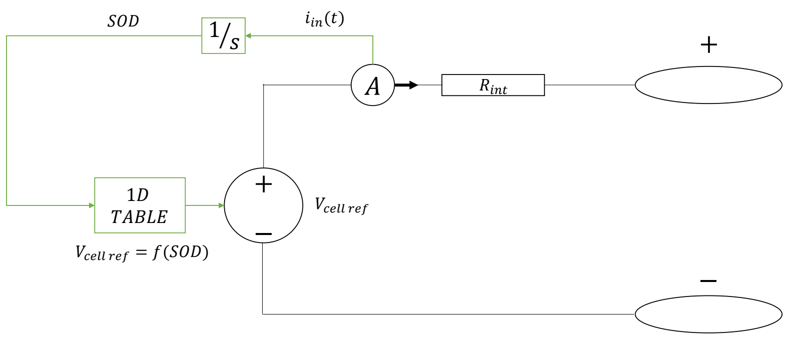

Figure 5.7: Battery Model implemented for Average Simulation.

Two battery pack models were considered for the simulation with the data needed for the simulation shown below:

TOSHIBA $SCiB^{TM}$ PARAMETERS	
V_{cell}	2.3 V
C	23 Ah
R_{int}	1mΩ

Table 5.1: Main Parameters of TOSHIBA $SCiB^{TM}$.

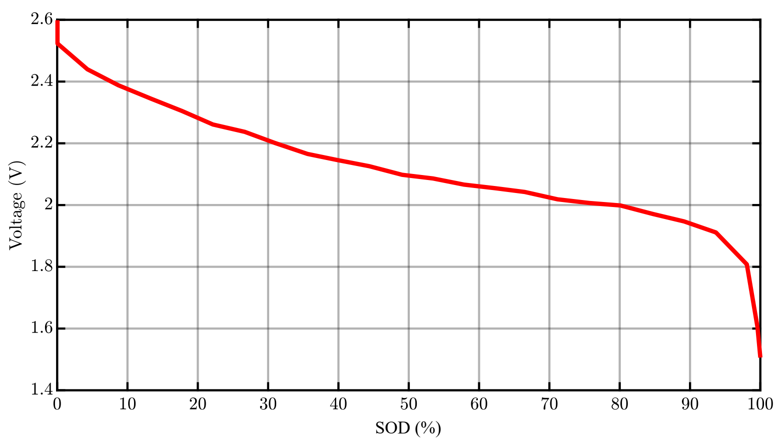

Figure 5.8: TOSHIBA $SCiB^{TM}$ Cell Characteristics.

REPT PARAMETERS	
V_{cell}	3.65 V
C	155 Ah
R_{int}	0.6mΩ

Table 5.2: Main Parameters of REPT.

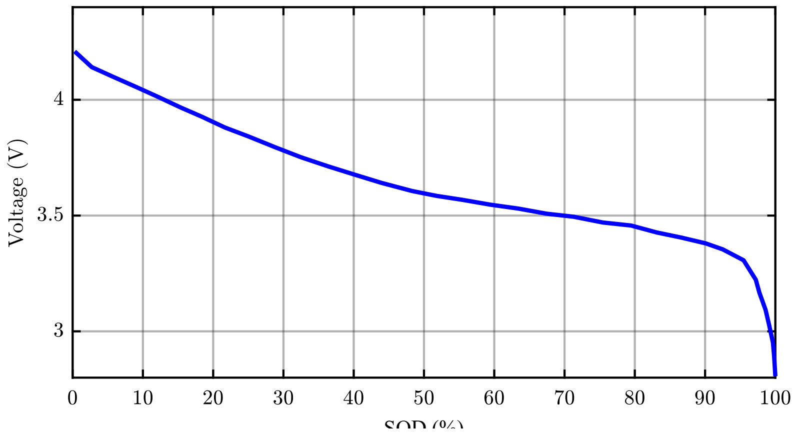

Figure 5.9: REPT Cell Characteristics.

5.3 Simulation Results

Simulations were carried out on various load diagrams with different conditions and module so as to test the control algorithm in various cases.

5.3.1 Simulations of Identical Modules with same SOC

In this simulation, three identical battery packs from Toshiba were simulated with each other in a manner over various cycles to see their response to various load diagrams. The initial simulation parameters are shown in Table 5.3

SIMULATION PARAMETERS	
V_{out}^{*}	1000V
V_{batt}	400 V
Module	TOSHIBA $SCiB^{TM}$
Number of Module	3
n_s	174
n_p	90
SOC_1	100%
SOC_2	100%
SOC_3	100%
C	1 mF
R	10mΩ
L	1.7 mH
ω_i	$800 \cdot 2\pi\ rad/s$
$K_{p,i}$	$w_b L$
$K_{i,i}$	$0.1 w_b \cdot K_p$
ω_V	$10 \cdot 2\pi\ rad/s$
$k_{p,V}$	$\cdot \omega_b C$
$K_{i,V}$	$0.1 \cdot \omega_b \cdot k_{p,V}$

Table 5.3: Main Parameters of the Ro-Ro Ferry Simulation.

The load diagram concerns a ferry vessel used for transporting wheeled vehicles or unloading/loading cargo also transported by means of wheeled vehicles. The load diagram and SOC trend of the three modules are shown in Fig. 5.10. As it can be seen, the trend is identical for all three modules.

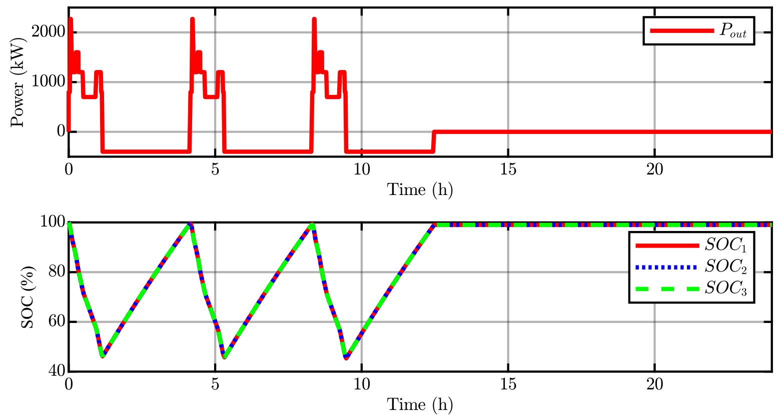

Figure 5.10: P_{out} and SOC for a Ro-Ro Ferry Vessel

A second simulation was carried out considering a different load chart, this time one of a passenger vessel with a lower load chart than the previous one. The parameters of this second simulation are shown in Table 5.4. The results are shown in Fig.5.11. Again the modules work the same way due to the same initial conditions, always maintaining the same SOC.

SIMULATION PARAMETERS	
V^*_{out}	1000V
V_{batt}	400 V
Module	TOSHIBA $SCiB^{TM}$
Number of Module	3
n_s	174
n_p	10
SOC_1	100%
SOC_2	100%
SOC_3	100%
C	1 mF
R	10mΩ
L	1.7 mH
ω_i	$800 \cdot 2\pi\ rad/s$
$K_{p,i}$	$w_b L$
$K_{i,i}$	$0.1\ \ w_b K_p$
ω_V	$10 \cdot 2\pi\ rad/s$
$k_{p,V}$	$\omega_b C$
$K_{i,V}$	$0.1\omega_b k_{p,V}$

Table 5.4: Main Parameters of the Urban Ferry Simulation.

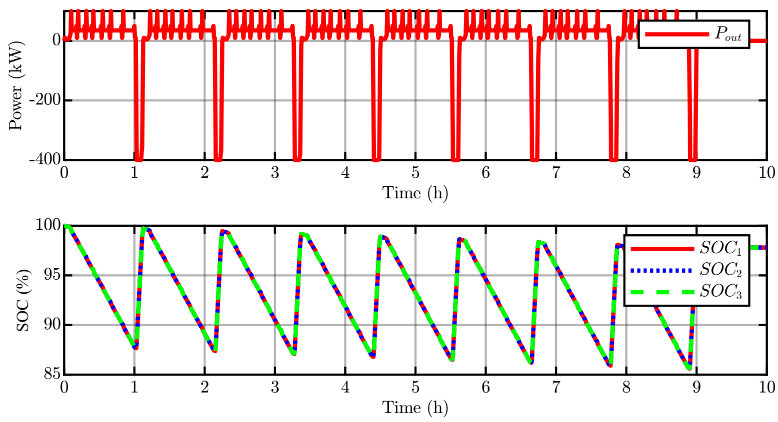

Figure 5.11: P_{out} and SOC for a Urban Ferry Simulation.

5.3.2 Simulations of Identical Modules with different SOC

For this simulation, all the parameters have been kept except the initial SOCs of the three modules in order to see how the system responds to this different initial condition. The results are shown in Fig. 5.12

SIMULATION PARAMETERS	
V^*_{out}	1000V
V_{batt}	400 V
Module	TOSHIBA $SCiB^{TM}$
Number of Module	3
n_s	174
n_p	90
SOC_1	100%
SOC_2	70%
SOC_3	80%

Table 5.5: Main Parameters of the Ro-Ro Ferry Simulation with different initial SOC.

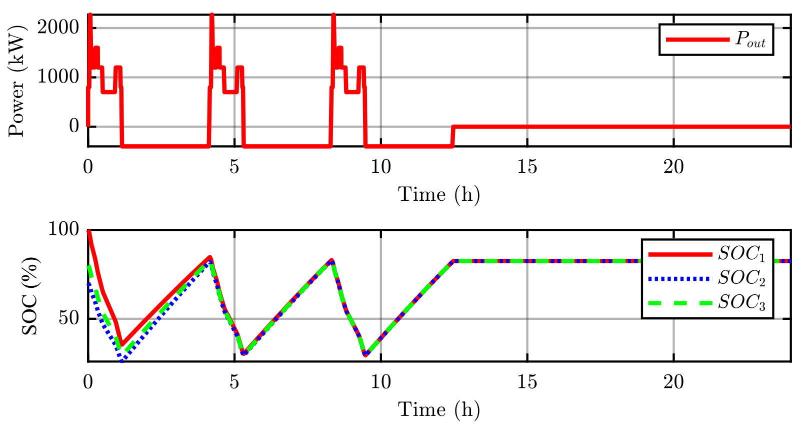

Figure 5.12: P_{out} and SOC for a Ro-Ro Ferry Vessel with different SOC.

SIMULATION PARAMETERS	
Module	TOSHIBA $SCiB^{TM}$
Number of Module	3
n_s	174
n_p	10
SOC_1	100%
SOC_2	70%
SOC_3	80%

Table 5.6: Main Parameters of the Urban Ferry Simulation with different initial SOC.

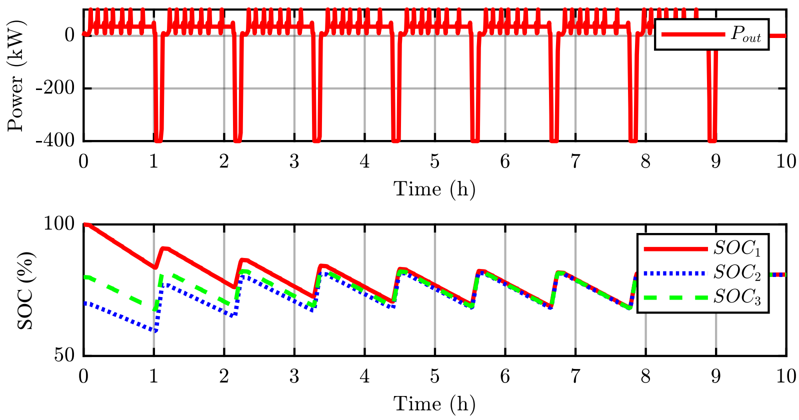

Figure 5.13: P_{out} and SOC for a Urban Vessel with different SOC.

As can be seen, the system responds to the different initial SOCs by exploiting the modules in a different way and proportional to their state of charge until a correct equalization and exploitation of the various modules is achieved.

5.3.3 Simulations of Different Modules with different SOC

In this simulation, one of the Toshiba modules has been replaced with one from the REPT, with different parameters compared to the first two and different initial SOC between the various modules in order to see the behavior of the system at this new configuration. The parameters of the Ro-Ro vessel simulations implemented are shown in Table 5.7 And the SOC trends in Fig.5.14

SIMULATION PARAMETERS	
Module 1	TOSHIBA $SCiB^{TM}$
n_s	174
n_p	10
Module 2	TOSHIBA $SCiB^{TM}$
n_s	174
n_p	10
Module 3	REPT
n_s	115
n_p	15
SOC_1	100%
SOC_2	70%
SOC_3	80%

Table 5.7: Main Parameters of the Ro-Ro Ferry Simulation with different Modules.

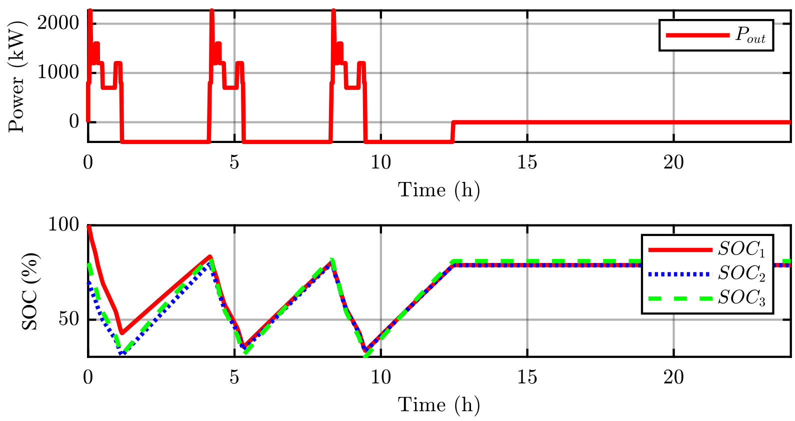

Figure 5.14: P_{out} and SOC for a Ro-Ro Ferry Vessel with different Modules.

SIMULATION PARAMETERS	
Module 1	TOSHIBA $SCiB^{TM}$
n_s	174
n_p	10
Module 2	TOSHIBA $SCiB^{TM}$
n_s	174
n_p	10
Module 3	REPT
n_s	115
n_p	15
SOC_1	100%
SOC_2	70%
SOC_3	80%

Table 5.8: Main Parameters of the Urban Ferry Simulation with different Modules.

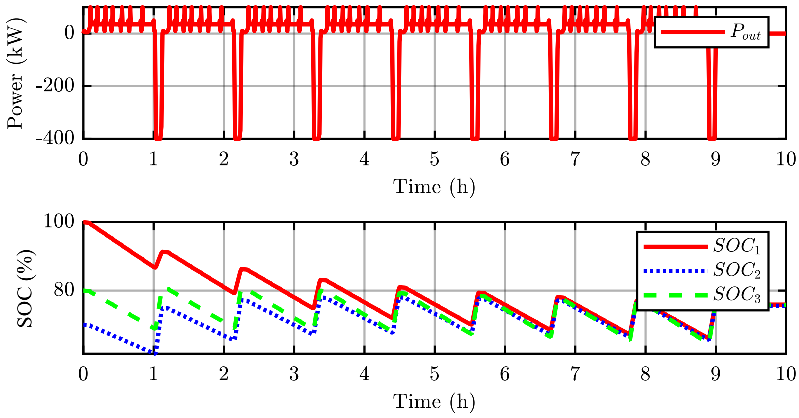

Figure 5.15: P_{out} and SOC for a Urban Ferry Vessel with different Modules.

Despite the different Capacity and SOC modules, the control still manages to adequately exploit the various modules allowing their optimal exploitation and the achievement of very similar SOCs at the end of each simulated work cycle.

Chapter 6

Conclusions

In this thesis, modular structure formed by an array of modules each consisting of a battery pack and its own converter was studied. This structure will be implemented in naval applications so as to reduce emissions and increasingly lead to the complete electrification of the maritime sector. A possible control algorithm of the system current loop has been studied that, in addition to correctly following the reference, will exploit the batteries properly taking into account the SOC, capacity and other characteristics of each module adapting the duty cycle accordingly so as to have a proper exploitation of the batteries under various conditions. A control code was implemented and tested on a scaled system to verify its operation under various working conditions with good results regarding the exploitations of the various modules. A traditional control was compared with a PS-PWM control. The latter brought excellent benefits concerning current ripple and output filter sizing compared with the traditional one. The use of a PS-PWM control coupled with the high modularity of the system makes the sizing of the output filters easier and less onerous but requires efficient communication between the various modules in order to keep the system synchronous. The high modularity of the system makes it usable for various applications with different power and voltage levels.

6.1 Personal Contribution

My personal contribution can be summarized as:

- Literature review about Energy Storage System and Ships Architecture.
- Study of the differences between centralized and distributed storage systems.
- Study of the operation and control of a Modular Converter.
- Study of a control that takes into account the various parameters of the batteries used
- Implementation of the control algorithm in C language for a string of modules.
- Comparison of a PWM and PS-PWM control.
- Simulations of a scaled-up system to verify its operation
- Simulation of a scaled system and analysis of its response to a real load diagram

Bibliography

[1] Luona Xu et al. “A Review of DC Shipboard Microgrids Part I: Power Architectures, Energy Storage and Power Converters”. In: *IEEE Transactions on Power Electronics* (2021).

[2] Iustin Radu Bojoi, ed. *Dispense corso di Elettrinica di Potenza*. 2022.

[3] Iustin Radu Bojoi, ed. *Dispense corso di Azionamenti Elettrici*. 2019.

[4] Gianmario Pellegrino, ed. *Dispense corso di Laboratory of Power Converters and Electrical Drives*. 2021.

[5] J Schonberger. “Modeling a lithium-ion cell using PLECS”. In: *Plexim GmbH* (2009), pp. 1–5.

[6] Nilanjan Mukherjee and Dani Strickland. “Control of second-life hybrid battery energy storage system based on modular boost-multilevel buck converter”. In: *IEEE Transactions on Industrial Electronics* 62.2 (2014), pp. 1034–1046.

[7] Shunfeng Yang, Yi Tang, and Peng Wang. “Distributed control for a modular multilevel converter”. In: *IEEE Transactions on power Electronics* 33.7 (2017), pp. 5578–5591.

[8] Paul Dan Burlacu, Laszlo Mathe, and Remus Teodorescu. “Synchronization of the distributed PWM carrier waves for modular multilevel converters”. In: *2014*

International Conference on Optimization of Electrical and Electronic Equipment (OPTIM). IEEE. 2014, pp. 553–559.

[9] D Grahame Holmes and Thomas A Lipo. *Pulse width modulation for power converters: principles and practice*. Vol. 18. John Wiley & Sons, 2003.

[10] Wangxin Huang and Jaber A Abu Qahouq. “Energy sharing control scheme for state-of-charge balancing of distributed battery energy storage system”. In: *IEEE Transactions on Industrial Electronics* 62.5 (2014), pp. 2764–2776.